# Chapter 8

# Magnetic Self-Assembling of Spherical Co Nanoparticles Used as Building Blocks: Syntheses, Properties and Theory

**Johannes Richardi, C. Petit, and Isabelle Lisiecki**

**Abstract** In this chapter, we show that thanks to the use of micellar and organometallic approaches, one can favor the growth of uniform spherical Co NPs with controlled surface passivation (dodecanoic acid or oleylamine), tunable size (from around 4 to 9 nm) and tunable nanocrystallinity (from fcc to hcp structure). As a result of the balance between van der Waals attractions between the metallic NPs, magnetic interactions between the magnetic NPs and solvent-mediated interactions between ligands, these uniform colloidal NPs can be used as building units to form a full set of assemblies which morphology depends on the deposition strategy, involving solvent evaporation. In the case of spontaneous self-assembling of magnetic NPs, compact hexagonal 2D arrays and 3D superlattices called supercrystals can form. In the latter case, either face-centered cubic supercrystalline films or single colloidal crystals can be obtained. Mesostructures of hexagonally ordered columns, labyrinths and void structures can result from assisted self-assembling, induced by the application of an external magnetic field. In highly ordered superlattices, individual NPs act as “artificial atoms” and occupy the lattice sites to form repetitive, periodic “artificial planes". From a fundamental point of view, these artificial solids constitute good models for investigating crystallization behavior. Resulting from collective interactions between neighboring NPs, they exhibit novel magnetic properties. The magnitude of these interactions, and then, the magnetic properties, can be tuned by various parameters including (1) the (crystallographic) nature of the magnetic NP, (2) the NP size, (3) the nature of the coating agent, (4) the nature

---

J. Richardi (✉)
Sorbonne Université, CNRS, Laboratoire de Chimie Théorique, LCT, F. 75005 Paris, France
e-mail: johannes.richardi@sorbonne-universite.fr
URL: https://www.lct.jussieu.fr/pagesperso/richardi/jrichardi.html

C. Petit · I. Lisiecki (✉)
Sorbonne Universités, UPMC Univ Paris 06, UMR 8233, MONARIS, 75005 Paris, France
e-mail: isabelle.lisiecki@upmc.fr

C. Petit
e-mail: christophe.petit@upmc.fr

J. Richardi · C. Petit · I. Lisiecki
CNRS, UMR 8233, MONARIS, 75005 Paris, France

D. Peddis et al. (eds.), *New Trends in Nanoparticle Magnetism*,
Springer Series in Materials Science 308,
https://doi.org/10.1007/978-3-030-60473-8_8

of the solvent, (5) the evaporation rate and (6) if appropriate, the application of an external field during the solvent evaporation. On the one hand, simulations based on a flory-type solvation theory using Hansen solubility colloidal parameters allow to predict the cobalt NP size. On the other hand, Monte Carlo simulations and free energy theories are able to predict the size and type of patterns appearing during the evaporation of a solution of magnetic NPs under a magnetic field.

## 8.1 Introduction

Self-assemblies of inorganic nanoparticles (NPs) into micrometer-scale ordered arrays and original mesostructures constitute a new generation of advanced materials [1–3]. Depending on the deposition strategy, involving solvent evaporation of a colloidal solution, various types of assemblies can be obtained. In the case of spontaneous self-assembling of magnetic NPs (MNPs), compact hexagonal 2D arrays [4, 5] and 3D superlattices called supercrystals [6] can form. Mesostructures of hexagonally ordered columns, labyrinths and void structures can result from assisted self-assembling, induced by the application of an external magnetic field [7]. In highly ordered superlattices, individual NPs act as “artificial atoms” and occupy the lattice sites to form repetitive, periodic “artificial planes". From a fundamental point of view, these artificial solids constitute good models for investigating crystallization behavior. In addition, their properties are determined by both individual NPs and their collective interactions. Resulting from collective interactions between neighboring NPs, they exhibit new mechanical, [8] transport, [9] optical, vibrational, [10] chemical (stability against oxidation and coalescence) and magnetic properties [11].

Fundamentally, one of the prerequisites to create assembly into well-defined superstructures is the use of NPs with uniform size and shape. The necessary conditions to form such populations are (1) a short nucleation step followed by (2) a slower growth step of the nuclei. Focusing on cobalt, size-controlled colloidal synthesis of spherical metallic NPs, remains, to this day, challenging. Such uniform MNPs have to be characterized by a high stability against oxidation and coalescence but not only. Regarding to the applications, high anisotropy of NPs is mainly required, it is then crucial to obtain preferentially highly crystallized hcp-Co NPs, rather than the two other possible structures, i.e., epsilon and fcc ones. The existing strategies to address these challenges are based on decomposition of organometallic precursors and metal-salt reduction, including the micellar method. In the case of decomposition of organometallic precursor, a precursor (e.g., $Co_2(CO)_8$) is rapidly decomposed at high temperatures in presence of surfactants and the NP size is tuned by tailoring the reaction time, reaction temperature, precursor injection time, surfactant to precursor ratio and chemistry of reagents and surfactants. For Co, this approach has been initiated by Dinega and Bawendi who obtained epsilon-Co NPs with however a rather high size polydispersity [12]. The first example of uniform size and shape tunable Co NPs using this approach has been reported by Puntes et al. [13] who obtained epsilon-Co NPs coexisting however with hcp-Co nanodisks. Thereafter, keeping unchanged the precursor but varying the surfactants, populations of tunable size have been obtained characterized by either epsilon [13], fcc [14] or a mixing of hcp/fcc [15] structure. Another approach for formation of size-controlled spherical Co NPs is the reduction approach. In this method typically, a reducing agent is injected into a hot solution of metal-salt precursor either inorganic or organic ($CoCl_2$ or $Co(CH_3COO)_2$) in the presence of surfactants. Inorganic metal-salt chemical reduction first reported by Murray and Sun [16] allows the formation of uniform size tunable epsilon-Co NPs [14]. The group of Chaudret, using an organic metal-salt as precursor, Co(η3-C8H13)(η4-C8H12), that readily decomposes at lower temperature (around 150 °C) under a pressure of dihydrogen (usually 3 bars), synthesized Co NPs with an fcc/hcp structure [17]. Using a variant of the inorganic metal-salt reduction where the reducing agent also plays the role of the solvent (polyol method), Murray et al. published the first example of hcp-Co NPs. Recently, Mezziane et al. developed a simple organometallic approach based on the combination of oleylamine and $ClCo(PPh_3)_3$ and evidenced the formation of pure monodisperse spherical hcp-Co NPs, ferromagnetic at room temperature [18]. The reduction in reverse micelles, performed at room temperature, also allows the formation of uniform size tunable Co NPs, characterized by an fcc polycrystalline structure [19–21]. Using the appropriate annealing treatment and taking advantage of their high thermal stability, Co polycrystals can transform into hcp single-crystalline NPs [22, 23]. For all these approaches, surfactant is a key parameter not only to stabilize the NPs against coalescence and oxidation but also to mediate the NP growth.

The assembly of NPs can be obtained through the evaporation of a colloidal solution. As a result of the balance between van der Waals attractions between the metallic NP, magnetic interactions between the MNPs and also solvent-mediated interactions between ligands, uniform colloidal MNPs can assemble into various mesostructures. The magnitude of these interactions can be tuned by various parameters including (1) the nature of the MNP, (2) the NP size, (3) the nature of the coating agent, (4) the nature of the solvent (5) the evaporation rate and (6) if appropriate, the application of an external field during the solvent evaporation. In the absence of external field, MNPs can self-assemble into 2D and 3D ordered arrays. The first reports of nanocrystal superlattices were published by Bentzon [24, 25] and coworkers in 1989 with iron oxide NPs used as building blocks. Then after, significant progress has been made in preparing long-range 2D and 3D superlattices of MNPs. 2D superlattices composed for example of spherical MNPs (Co [6], Ni [26], Fe [27] and $Fe_2O_3$ [28]), are characterized by a hexagonal packing and can be obtained at the micrometer scale. Besides, self-organization of MNPs into 3D supercrystals has been, however in a less extend, evidenced by several groups. Depending on the experimental conditions, two growth processes are observed (1) onto a substrate (heterogeneous nucleation and growth) or (2) in solution (homogeneous nucleation and growth). In the first case, film morphology is obtained whereas in the latter ones, the colloidal crystals obtained are characterized by well-defined shape. The first example of long-range ordered 3D supercrystal film of MNPs has been published in 2003 by Lisiecki et al. [6]. These artificial solids are made of several hundred monolayers of fcc-Co NPs, which order in an fcc “super” structure. 3D supercrystal films have been also obtained using Ni

[26], magnetite [28] and $Fe_3O_4$ [29] NPs. Even more rarely, only some colloidal crystals made of MNPs have been, at this day, reported in the literature, which can be attributed to the difficulty to meet all the conditions to growth them. They have been obtained using Ni [26], $\gamma$-$Fe_3O_4$-$Fe_2O_3$ [30] and $Fe_3O_4$ [29].

Physico-chemical properties, especially magnetic ones of assemblies of NPs, are known to be significantly impacted by a set of parameters including (1) MNP size, (2) nanocrystallity, (3) interparticle gap, (4) degree and type of ordering of the superlattice, (5) morphology. In this chapter, we cover the results obtained in our group on (1) the colloidal synthesis of uniform and spherical cobalt NPs, (2) their use for the elaboration of 2D and 3D assemblies by means of spontaneous and assisted assembling and (3) their magnetic properties. The key factors for the synthesis of uniform Co NPs and their assemblies will be discussed. We will also present theories and simulations, which predict the size and shape of mesostructures obtained from evaporation of MNP solutions under a magnetic field.

## 8.2 Synthesis of Uniform Spherical Co Nanoparticles

### *8.2.1 Synthesis by Micellar Approach*

#### 8.2.1.1 Cobalt Nanoparticle Size Polydispersity Control

Co NPs are synthesized by solution-phase reduction approach, at room temperature [20]. The precursor used is the cobalt (II) bis(2-ethylhexyl) sulfosuccinate, $Co(AOT)_2$. $5 \times 10^{-2}$ M $Co(AOT)_2$ solution is prepared using isooctane as bulk solvent [31]. The amount of water concentration defined as $w = [H_2O]/[AOT] = 32$. This prepared microemulsion is vigorously shaken for a few minutes for equilibrium and form reverse micelles [32]. The reducing agent used is sodium tetrahydroborate, and its concentration is given by $R$ ($R = [NaBH_4]/[Co(AOT)_2]$). $R$ value varies from 0.5 to 8 by varying the volume of a fixed concentration ($[NaBH_4] = 1$ M) added to the micellar solution. Under vigorous shaking, the solutions instantaneously turn from pink to black indicating the formation of Co NPs. Above $R = 0.5$, resulting from the large amount of water brought by the reducing agent injected, reverse micelles are instantaneously destroyed [32, 33]. After the synthesis, whatever the $R$ value is, Co NPs are extracted from the AOT surfactant by adding highly concentrated dodecanoic acid solution ($[C_{12}H_{25}COOH] = 0.2$ M). After washing several times with ethanol, the NPs are dispersed in hexane and then centrifuged to precipitate bulky material. Only the upper phase containing dodecanoic acid coated NPs is collected. All the steps are carried out in a nitrogen glove box using deoxygenated solvents to prevent metal oxidation. Transmission electron microscopy (TEM) investigation is performed after depositing some drops of the colloidal solutions onto a carbon TEM grid and complete evaporation of the solvent. As can be observed in TEM images (Fig. 8.1), the populations of NPs significantly depend on $R$ value. At $R =$

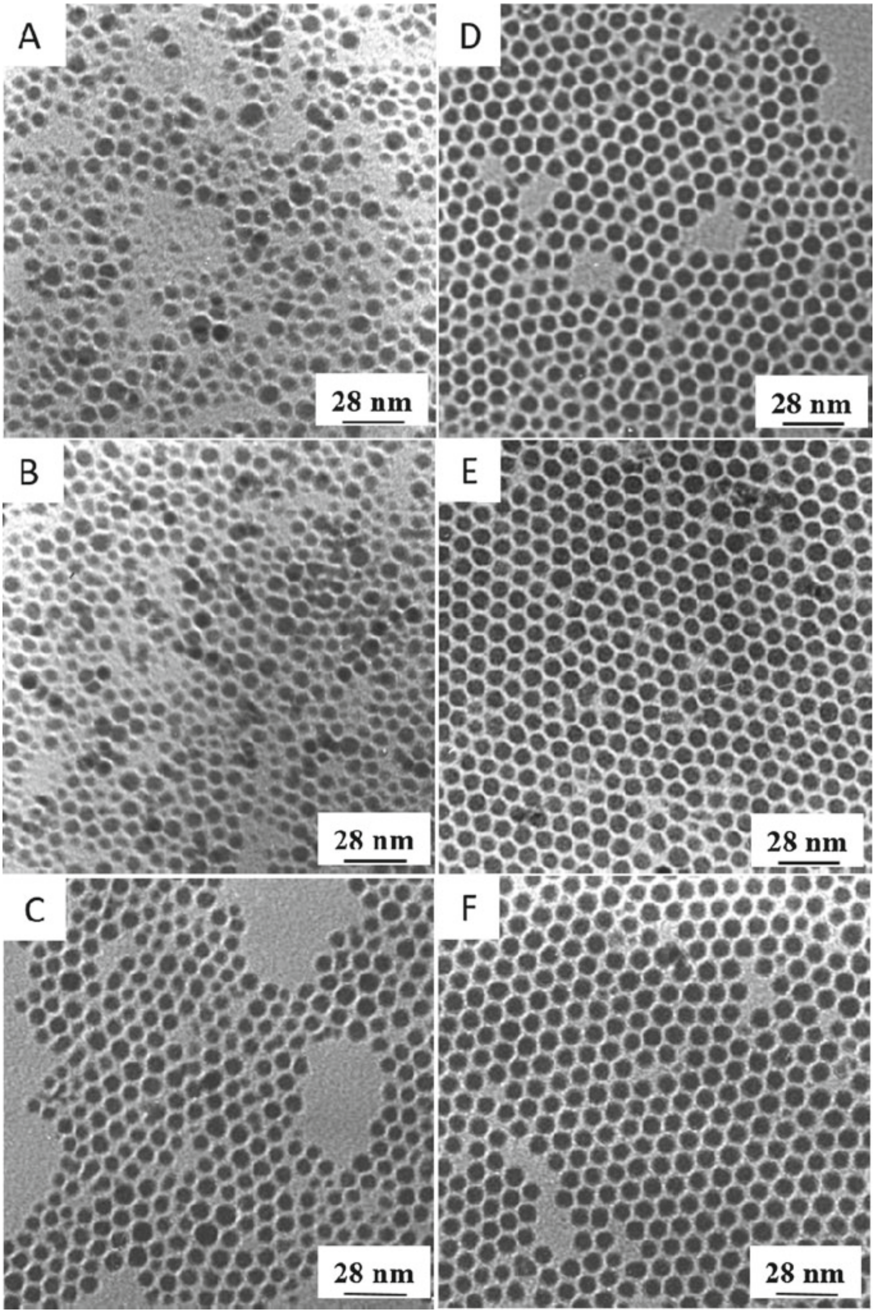

**Fig. 8.1** TEM images of cobalt nanoparticles synthesized by the micellar approach, at various sodium tetrahydroboride concentrations, $R$. **a** ($R = 0.5$), **b** ($R = 1$), **c** ($R = 2$), **d** ($R = 4$), **e** ($R = 6$) and **f** ($R = 8$)

**Table 8.1** Average diameter of Co nanoparticles *D*, and size distributions, $\sigma$, at various *R* values

| *R* | 0.5 | 1 | 2 | 4 | 6 | 8 |
|---|---|---|---|---|---|---|
| *D* (nm) | 6 | 7 | 7 | 7 | 7 | 8 |
| $\sigma$ (%) | 30 | 18 | 13 | 12 | 12 | 8 |

0.5, the mean diameter is 6 nm (Table 8.1), with a large size polydispersity, around 30%. By increasing *R* value, the more important change is the decrease in the size polydispersity which drops from 30 to 8%. In a lesser extend, the mean diameter slightly increases from 6 to 8 nm. Such feature is attributed to the increase in the yield of the reduction reaction that is not complete below $R = 8$ [34]. This statement is well illustrated by the concentration increase of the colloidal solution, by a factor of almost 5, when *R* increases from 0.5 to 8. Higher the *R* value, larger the NP diameter. The mean diameter increase combined to the size selection occurring at the end of the synthetic process explains the reducing agent concentration effect. This result shows that the best condition to promote the growth of uniform Co NPs, initiating in AOT reverse micelles, is to work in a saturation regime in reducing agent.

### 8.2.1.2 Cobalt Nanoparticle Size Control

Revisiting the chemical reduction approach of $Co(AOT)_2$ precursor presented below, a novel strategy based on the change of the bulk solvent gives rise to uniform colloidal Co NPs with tunable size [21]. Six different micellar solutions of $5 \times 10^{-2}$ M $Co(AOT)_2$ are prepared using xylene (sample S1), cyclohexane (sample S2), cumene (sample S3), decane (sample S4), octane (sample S5) and isooctane (sample S6). *w* value is fixed at 2. Whatever the bulk solvent is, reverse micelles form [32–36]. Taking into account the importance of the saturation in reducing agent on Co size polydispersity, *R* value is fixed at 6. The rest of the protocol is similar to the previous one. At the end of the synthesize, six colloidal solutions with dodecanoic acid ($C_{12}$) coated Co NPs are obtained with hexane used as solvent. For clarity, this latter solvent is called "$C_{12}$-NP solvent" against "AOT solvent" for the initial bulk solvent use to form initial reverse micelles. TEM investigation performed on the six populations of Co NPs reveals that the growth of Co NPs drastically depends on the nature of the AOT solvent (Fig. 8.2 and Table 8.2). Indeed, the mean diameters of Co NPs for xylene, cyclohexane, cumene, decane, octane and isooctane are found equal to 3.9, 4.6, 4.7, 7.0, 7.6 and 7.7 nm, respectively. It is noticeable that all the samples are characterized by a rather low size polydispersity, i.e., around 12%. Co NP synthesize is occurring in an out-of-equilibrium ternary component system composed of $Co(AOT)_2$, oil and water. Despite the complexity of such a reaction system, size control of Co NPs can be explained by solvent-mediated AOT-AOT interactions. The NP formation is separated into two steps, (1) the nucleation step and (2) the growth step. The nucleation step mainly depends on the Co–Co interactions. DFT calculations show that the interactions between the solvent and the cobalt atoms are significantly weaker than the Co–Co interactions [37]. Therefore, an eventual

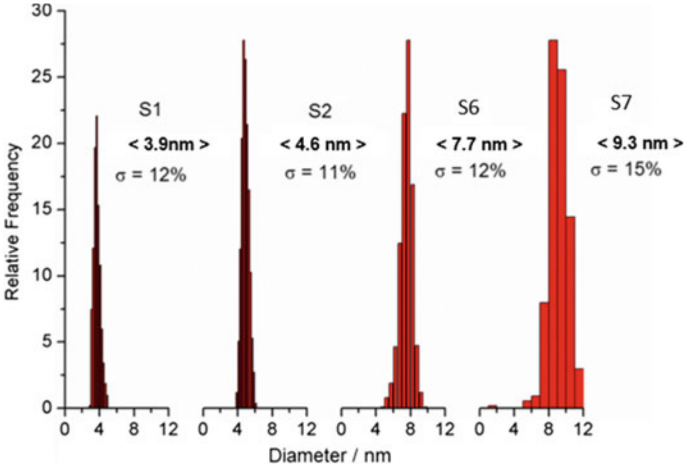

**Fig. 8.2** Size distribution of Co nanoparticles synthesized by the micellar approach with different combinations of AOT solvent/$C_{12}$-NP solvent: xylene/hexane (S1), cyclohexane/hexane (S2), isooctane/hexane (S3) and isooctane/cyclohexane (S4)

**Table 8.2** Average diameter ($D$) and size distribution ($\sigma$) of Co NP populations obtained with various solvent-ligand pairs used in the experiments. $\chi_{12}$ is the interaction parameter calculated for the various solvent-ligand pairs

| Solvent-ligand (sample) | $D$ (nm) | $\sigma$ (%) | $\chi_{12}$ (J mol$^{-1}$) |
|---|---|---|---|
| Octane—AOT (*S5*) | 7.6 | 11 | 0.02375 |
| Isooctane—AOT (*S6*) | 7.7 | 12 | 0.02412 |
| Decane—AOT (*S4*) | 7.0 | 12 | 0.05058 |
| Cyclohexane—AOT (*S2*) | 4.6 | 11 | 0.17272 |
| Cumene—AOT (*S3*) | 4.7 | 11 | 0.44645 |
| Xylene—AOT (*S1*) | 3.9 | 12 | 0.49455 |
| Hexane—C12 (*S6*) | 7.7 | 12 | 0.06424 |
| Cyclohexane—C12 (*S7*) | 9.3 | 15 | 0.03062 |

impact of the solvent on the nucleation can be ruled out. However, the growth of NP is driven by the AOT adsorption on the metal surface through the attractions between the cobalt atoms and the polar head groups of AOT but also by AOT/AOT interactions [38]. Changing the nature of the solvent impacts the AOT solvation and then the AOT/AOT interactions, that in turn, the final NP size. This statement is supported by the calculation of interaction parameters $\chi_{12}$ for the various solvent-AOT pairs, using the Hansen solubility parameters [21]. In Fig. 8.3, the NP diameter is plotted against the $\chi_{12}$ parameter using a logarithmic scale. It can be seen that the NP size decreases as the $\chi_{12}$ parameter increases. A linear regression gives

$$\log(d) = 0.944 - 0.211 \log(c_{12})$$

**Fig. 8.3** Log–log plot of the experimental cobalt nanoparticle size and the interaction parameter

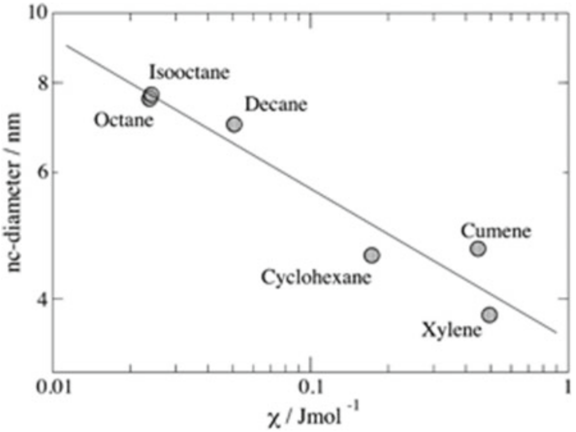

*d* and $\chi_{12}$ are expressed in nm and J $mol^{-1}$ respectively. Based on the experimental results, this formula yields the NP diameter within an error of around 1 nm.

For cyclohexane, xylene and cumene, the larger $\chi_{12}$ values favor the attraction between the AOT, resulting in the increase in the stability of the ligand layer and thus the hindering of the growth of the NPs. At the opposite, an increase in the $\chi_{12}$ value results in smaller NPs as observed for octane, isooctane and decane.

The importance of the interaction parameter on the NP size control is also well illustrated by the following experiment. After removing the upper hexane colloidal solution from sample S6, a part of the precipitate containing $C_{12}$-Co NPs, is dispersed in cyclohexane (*sample S7*). TEM study reveals that the mean diameter of this "second dispersion" is 9.3 nm against 7.7 nm for the first dispersion (in hexane). The size distribution slightly increases from 12 to 15% (Fig. 8.2 and Table 8.2). The $\chi_{12}$ parameter calculated for dodecane (used for dodecanoic acid) using cyclohexane is 0.0306 J $mol^{-1}$ against 0.0642 J $mol^{-1}$ for hexane used as solvents (Table 8.2). The lower $\chi_{12}$ value indicates that cyclohexane is a better solvent for $C_{12}$-NPs, thus hindering the particle aggregation. This explains that, in this case, extraction from the precipitate of larger NPs is occurring, conversely to the use of hexane.

This novel strategy using the solvent-mediated ligand interaction allows to control accurately the NP size, but also to use a unique ligand to stabilize the NPs, e.g., dodecanoic acid that covalently binds to the Co surface ensuring high stability against oxidation and coalescence processes. It is noticeable that such a strategy would provide an efficient guide in the choice of the solvent for controlling the NP size of any material.

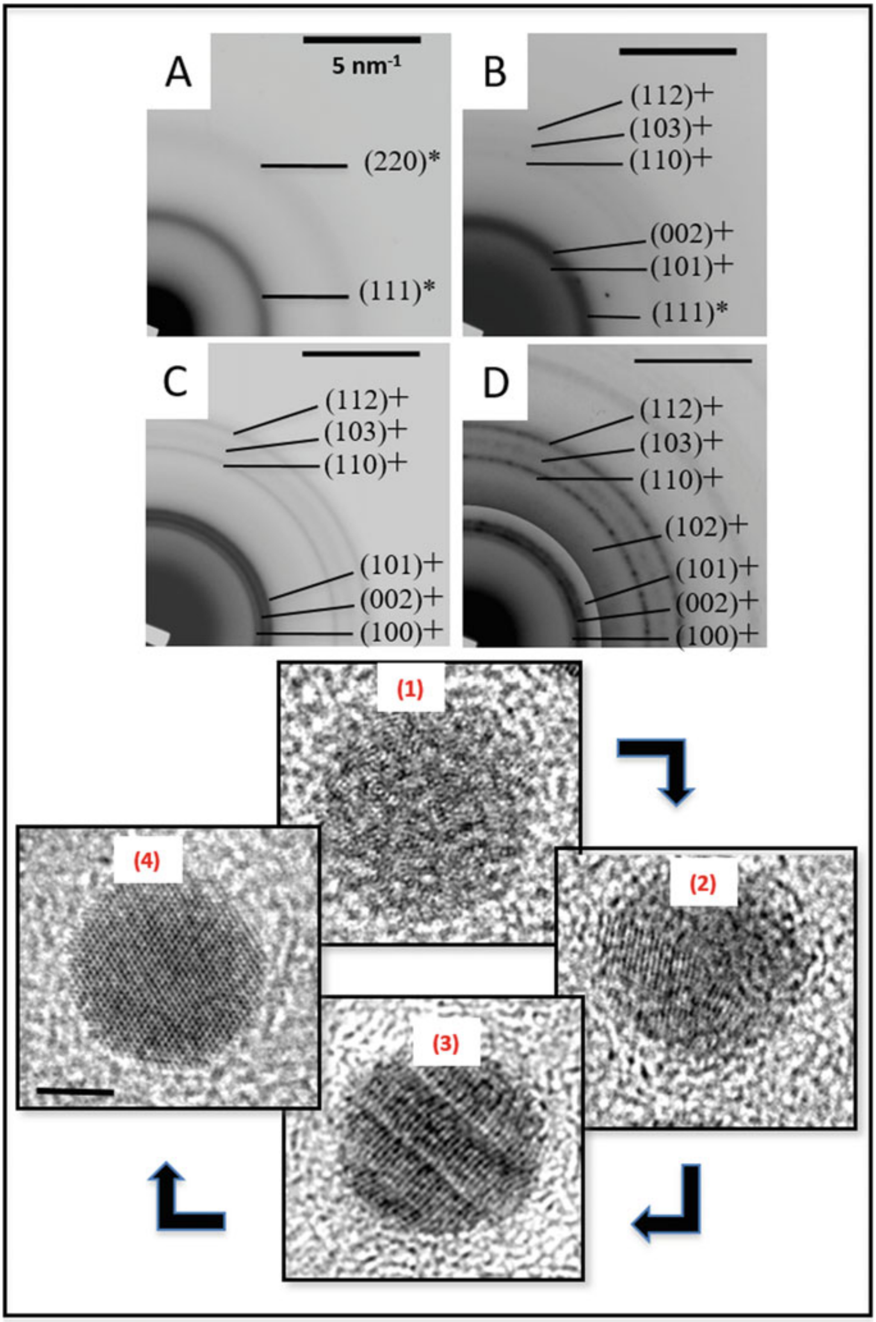

**Fig. 8.4** Electron diffraction patterns of 7.5 nm Co nanoparticles obtained by the micellar approach not annealed (**a**) and annealed at 250 °C (**b**), 300 °C (**c**) and 350 °C (**d**). Reflections corresponding to the fcc (*) and hcp (+) structures. (1–4) Representative HRTEM images of Co nanoparticles annealed at various temperatures

#### 8.2.1.3 Cobalt Nanoparticle Crystalline Structure Control

In order to improve the crystalline structure (nanocrystallinity) of the as-synthesized dodecanoic acid coated Co NPs (fcc polycrystals) obtained by the micellar approach, annealing treatments by (1) dry- and (2) solution-phase protocols are performed.

(1) Dry annealing is performed on 7.2 nm-NPs deposited on a TEM grid. The grid is placed in a close quartz ampule with a nitrogen atmosphere, finally placed in a furnace at various temperatures (250, 300 and 350 °C) for 15 min [23]. Electron diffraction and HRTEM (Fig. 8.4a, 4-1) reveal that the as-synthesized Co NPs are nearly amorphous with few ordered fcc domains less than 1 nm in size. After annealing at 250 °C, the structure is mainly hcp with some remaining fcc (Fig. 8.4b, 4-2). After annealing at 300 °C, pure hcp-Co NPs are obtained (Figs. 8.4c, 4-3), the defects of which tend to disappear at 350 °C (Figs. 8.4d, 4-4). Within error, the average diameter of the annealed NPs is unchanged.

(2) Recrystallization of fcc-Co into hcp-Co can be also driven by the solution-phase heating protocol. Using this novel strategy and conversely to the previous one, annealed NPs can be freely manipulated. Different protocols exist, always taking place in a refluxing bath, under nitrogen flux [2]. For instance, as-synthesized Co NPs are dispersed in high boiling point solvent, i.e., octyl ether. The solution is heated at 220 °C with a heating rate of 10 °C per minute up to 140 °C then more slowly with a heating rate of 2 °C per minute. Once the temperature is reached, NPs are maintained in the hot solution without aging or aged for 30, 90 and 180 min before a cooling step. Electron diffraction and HRTEM studies indicate the disappearance of the cfc phase just after reaching 220 °C, in favor of hcp-Co. After aging for 180 min, hcp-Co single crystals are obtained with a slight decrease in the mean diameter (6.5 nm against 7.2 nm for the native NPs).

Due to the high thermal stability of the dodecanoic acid coating, we show that dry- and solution-phase annealing treatments give rise to the structural transition from fcc-Co polycrystals to hcp-Co single crystals. No trace of Co oxide is detected. It is noticeable that reports in the literature of colloidal hcp-Co single crystals are very rare [14, 18].

## 8.3 Synthesis by Organometallic Approach

Besides the micellar soft chemical approach developed above, polyol synthesis of NPs appears to be one of the "simplest" routes to prepare NPs involving reduction of inorganic salt at high temperature (depending on the polyol) [39–41]. This is also the most representative approach of a complicated mixture synthesis of NPs as variations on the polyols, cobalt salt, surfactant, even bi-surfactant mixture, ruthenium seeds additive allow to reach different shapes, sizes and phases (mainly fcc-Co and hcp-Co) of nanocrystals [42–44]. As mentioned above, two other processes have been developed to produce monodispersed Co NPs in milder conditions using Co(0) or (I) organometallic precursors instead of inorganic. The first one is related to carbonyl metal complexes (CMC, $CO_2(CO)_8$) and their thermal decomposition to generate NPs [16, 18]. The second one is dealing with hydrocarbyl complexes (HC) such as $Co(\eta^3\text{-}C_8H_{13})$ $(\eta^4\text{-}C_8H_{12})$ that readily decompose at lower temperature under a high pressure of dihydrogen [17]. However, the use of carbon monoxide as ligand (CMC approach) or a pressure of hydrogen (HC approach) still requires specific equipment in the laboratory. Moreover, these organometallic precursors are not readily available on a large scale and often as for the micellar route, annealing is necessary to reach pure hcp-Co phases (See above).

Based on the cobalt(II) salt and the cobalt(0 or I) organometallic approaches, a novel strategy has been developed by using a well-defined cobalt (I) halide complexes ($ClCo(PPh_3)_3$) in presence of oleylamine (OAm) which should act as the solvent, the surfactant and as the reducing reagent [18]. Using this Co(I) complex heating in degassed OAm at 190 °C during 1 h, the formation of spherical monodispersed Co NPs is demonstrated by TEM study (Fig. 8.5). They are 9.2 nm spherical Co NPs, characterized by a very low size polydispersity of 6%. It is important to notice that no post-synthetic treatment is necessary to reach this control of the size distribution. TEM investigation allows a complete structural characterization of the cobalt NPs. A typical electronic diffraction pattern (Fig. 8.5A) obtained for a collection of NPs (Fig. 8.5c) consists of 7 diffractions rings characterized by 0.216 nm, 0.203 nm, 0.190 nm, 0.146 nm, 0.125 nm, 0.114 nm and 0.106 nm distances from center to outward, respectively. These distances correspond to the (100), (002), (101), (102), (110), (103) and (201) planes of the hcp structure of cobalt metal, when compared with the bulk values.

Magnetic characterization confirms the ferromagnetic behavior of these cobalt NPs even at room temperature, which is expected for these 9.2 nm in size hcp cobalt NPs [18, 45].

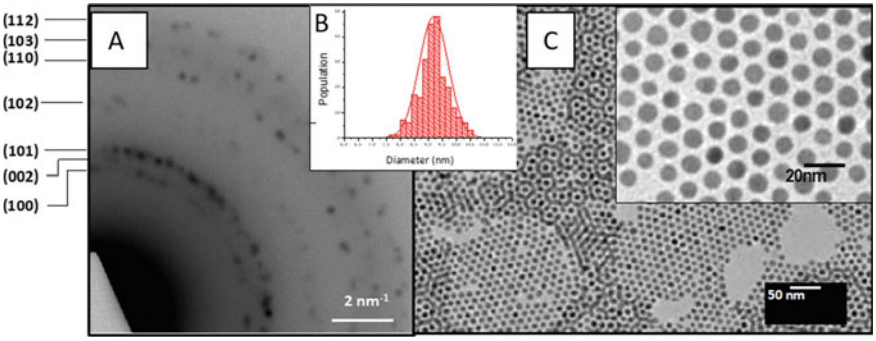

**Fig. 8.5** TEM characterization of 9.2 nm hcp cobalt nanoparticles obtained by the organometallic approach. **a** SAED, **b** size histogram, **c** TEM images

## 8.4 Assemblies of Cobalt Nanoparticles

### *8.4.1 Key Parameters Involved in the Nanoparticle Organization*

For a long time, experimentalists and theoreticians have sought the optimal conditions to obtain well-defined self-organization of NPs in 2D and 3D lattices. Here, we will focus on the self-assembly in solution. Three major parameters have become evident for this process: the speed of evaporation, the monodispersity of the particle size and the interaction between the NPs.

Concerning the *evaporation speed*, it has been observed that it has too be sufficiently small to allow the cluster of nanoparticles to come together to form mesostructures. This is usually empirically reached by a confinement of the beaker used for the evaporation.

Concerning the *monodispersity*, experiments have shown that well-ordered superlattices are observed at polydispersities lower than 5%, while polydispersities larger than 12% suppress ordered assemblies [46]. The theoretical study of solid–fluid transitions in hard-sphere systems using Monte Carlo simulations has given explanation for this observation [47, 48]. It reveals the existence of a terminal polydispersity above which, no crystallization can occur. The highest polydispersity is 5.7% for the solid and about 12% for the fluid. Fractionation enables a fluid of larger polydispersity to crystallize into several solids of smaller polydispersity and different average size. Therefore, a batch of nanocrystals synthesized with an average polydispersity smaller than 12% may form superlattices by fractionation, while within a large superlattice, the average polydispersity should be smaller than 6%. Simulations have shown that kinetic factors are the reason for the existence of the terminal polysdispersity [49]. Usually the free energy barrier to nucleation continuously decreases with increasing concentration enabling the formation of crystals. The simulations show that in polydisperse samples, the free energy barrier passes through a minimum, thus suppressing crystallization. Recent simulations have also shown that the fractionation may be a complex process [50]. We have carried out simulations in the 2D case using Lennard–Jones potential, which show this transition from an ordered to a disordered state when the polydispersity is increased. For a polydispersity of 6%, the left side of Fig. 8.6 shows an ordered assembly characterized by well-defined spots in the two-dimensional pair distribution function (see insert). This order disappears for a polydispersity of 15% on the right side of Fig. 8.6.

The third key parameter is the *interaction potential between the NPs*. To obtain a self-assembly purely by confinement due to the evaporation of the solvent, this interaction has to be repulsive even at the end of evaporation. In general, the interaction for two magnetic particles covered with chain-like ligands in a solvent may be expressed in the following way [51–53]:

$$u_{\mathrm{tot}}(r) = u_{vdW}(r) + u_{\mathrm{elastic}}(r) + u_{\mathrm{mix}}(r) + u_{\mathrm{ionic}}(r) + u_{\mathrm{dipole}}(r) \tag{8.1}$$

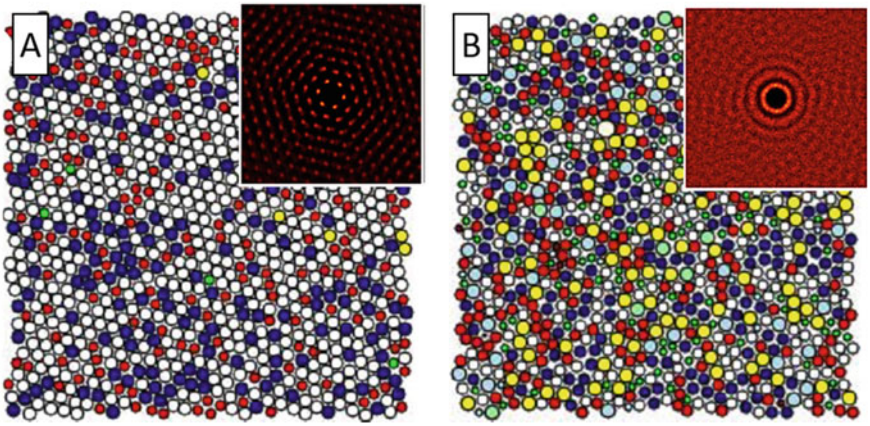

**Fig. 8.6** Snapshots of the final configuration of particle assemblies obtained by 2D Monte Carlo simulations for two polydispersities **a** 6%, **b** 15%. The different colors correspond to various particle sizes. The inserts show the two-dimensional pair distribution functions for the given particle assemblies

$u_{vdW}(r)$ corresponds to the van der Waals attraction between the cores of the particles. It is calculated from the effective Hamaker constant reduced with respect to its value in vaccuum due to the presence of the solvent medium. $u_{\mathrm{elastic}}(r)$ is the repulsion due to elastic compression of the ligands. $u_{\mathrm{mix}}(r)$ described the free energy due to the mixing of the thiol ligands, when the two particle approach. This is accompanied by a demixing of solvents and ligands. This term may be attractive or repulsive depending on the solvent. The equations for the last three terms are given in reference 53. When the nanoparticles are dissolved in an aqueous ionic solution, an additional repulsive term $u_{\mathrm{ionic}}(r)$ appears due to the formation of a cloud of counter-ions around charged nanoparticles. This can be for example described by a DLVO term or by the integral equation theories. Finally, we have the dipolar term $u_{\mathrm{dip}}(r)$ due to the magnetism of the particles, which can be estimated from the magnetization at saturation of the magnetic material. With the help of the code NanoForceG developed in our laboratory, the interaction potential in (8.1) can be easily calculated. In Fig. 8.7, the interaction potentials for cobalt nanoparticles coated with dodecanoic acid are shown. Figure 8.2a gives the potential for various nanoparticle sizes using decane as solvent. For particles smaller than 10 nm, the attraction between the nanoparticles is sufficiently weak to ensure the formation of well ordered assemblies. At larger nanocrystal size, the van der Waals interaction due to the metallic cores becomes important. Moreover, for size larger than 15 nm the dipolar term is sufficiently strong to influence the nanoparticle assembly. This may lead to the formation of chains, which have been experimentally observed for magnetic nanoparticles of this size [54–56]. In Fig. 8.7b, the influence of the solvent for cobalt nanoparticles of 5 nm is shown. As expected, the alkanes are good solvents which lead to a repulsion between the nanoparticles, while protic and polar solvents such as water and acetone are bad solvent. However, it is interesting to observe that there is an intermediate case,

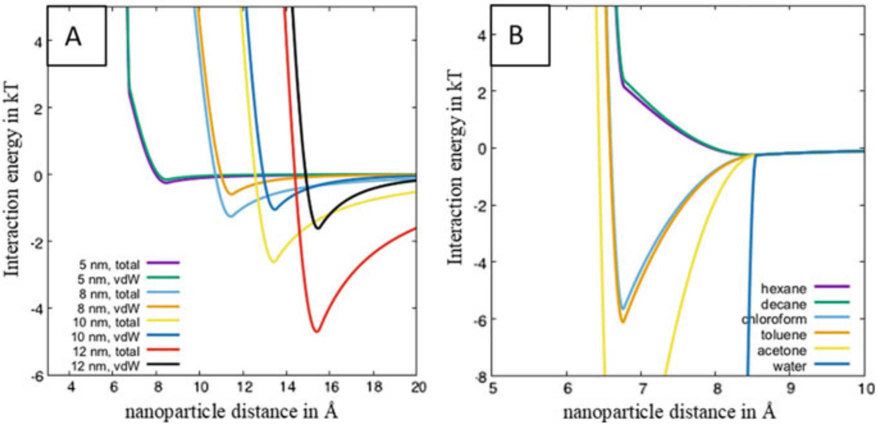

**Fig. 8.7** Interaction energy between cobalt nanoparticles coated with dodecanoic acid. Figure **A** shows the evolution with solvent for a nanoparticle size of 5 nm. Figure **B** gives the dependence on the nanocrystals size for decane as solvent. The total potential and the one without the dipolar term (denoted vdW) are plotted

neither really good nor bad, where solvents such as chloroform or toluene induce some attraction. This attractive force can be used to assemble the nanoparticle in a controlled way in the solution without evaporation of the solvent. Thus, well-defined supercrystals made of nanoparticles can be grown in solution [53, 54]. This opens up a new way to fabricate nanomaterials. We would conclude this section with a short discussion of the ionic term, which appears in aqueous solutions. During evaporation, the salt concentration increases which leads to a collapse of the ionic cloud and may induce an uncontrolled aggregation of the particle due to the van der Waals term. This explains why non-aqueous systems are usually preferred to obtain controlled nanoparticle assemblies. However, this does not exclude aqueous solutions of nanoparticles to obtain mesostructures. Under specific conditions, the formation of isolated chains has also been experimentally observed, which has been explained by simulations [57].

## 8.5 2D Self-Organizations of Cobalt Nanoparticles Synthesized by Micellar Approach

2D self-organizations of Co NPs are prepared by depositing 1 drop of a colloidal solution of either (1) as-synthesized fcc-Co polycrystals with various sizes 3.9 nm (S1), 4.6 nm (S2), 7.7 nm (S6), 9.3 nm (S7) or (2) solution-phase annealed 7.1 nm hcp-Co single crystals on a highly ordered pyrolytic graphite (HOPG) grid. The concentration of NPs is fixed at 5.5 $10^{-7}$ M. Subsequently to their deposition in

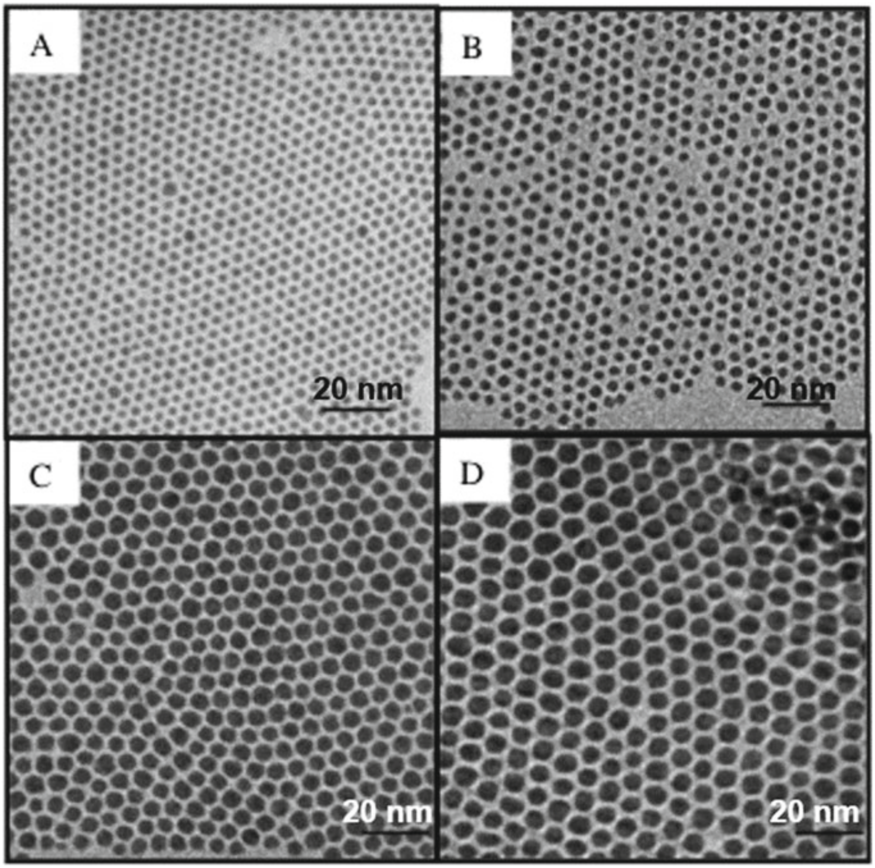

**Fig. 8.8** TEM images of 2D ordered arrays of native fcc-Co polycrystals obtained by the micellar approach **a** 3.9 nm (S1), **b** 4.6 nm (S2), **c** 7.7 nm (S6), **d** 9.3 nm (S7)

2D ordered arrays, the as-synthesized fcc-Co polycrystals can be submitted to a dry-annealing process (3).

(1) Whatever the size of the as-synthesized fcc-Co polycrystals, TEM study (Fig. 8.8a–d) shows the formation of 2D ordered arrays with hexagonal symmetry [21]. These organizations are determined by both the diameter and the length of the C12 coating agent. For 3.9 nm, the mean center-to-center distance between particles (Dc-c) and interparticle gap (Di-p) are 5.9 nm and 2.1 nm, respectively (Table 8.3). Taking into account length of dodecanoic acid in the cis–trans configuration, i.e., 1.77 nm, the low $D_{i\text{-}p}$ value indicates interdigitation between the C12 alkyl chains. The use of larger Co NPs, e.g., 4.6, 7.7 and 9.3 nm results in a significant decrease of the Di-p values found equal to 2.3, 1.6 and 1.4 nm, respectively. This behavior is attributed to the van der Waals attractions between the metallic core, which magnitude increases with the particle volume.

**Table 8.3** Structural characteristics of 2D ordered arrays presented in Figs. 8.5 and 8.6 and obtained by deposition of Co NPs characterized by an average diameter $D$ and a size distribution $\sigma$. $D_{c\text{-}c}$; center-to-center nanoparticle distance; $D_{i\text{-}p}$: inter-particle distance

| Sample | $D$ (nm) | $\sigma$ (%) | $D_{c\text{-}c}$ (nm) | $D_{i\text{-}p}$ (nm) |
|---|---|---|---|---|
| $\mathrm{Co_{fcc}}$ (*S1*) | 3.9 ± 0.1 | 12 | 5.9 ± 0.1 | 2.1 ± 0.1 |
| $\mathrm{Co_{fcc}}$ (*S3*) | 4.6 ± 0.1 | 11 | 6.9 ± 0.1 | 2.3 ± 0.1 |
| $\mathrm{Co_{fcc}}$ (*S6*) | 7.7 ± 0.1 | 12 | 9.3 ± 0.1 | 1.6 ± 0.1 |
| $\mathrm{Co_{fcc}}$ (*S7*) | 9.3 ± 0.1 | 15 | 10.5 ± 0.1 | 1.4 ± 0.1 |
| $\mathrm{Co_{hcp}}$ ($S_{ann}$ 1) | 7.1 ± 0.2 | 8 | 9.8 ± 0.2 | 2.7 ± 0.2 |
| $\mathrm{Co_{hcp}}$ ($S_{ann}$ 2) | 7.0 ± 0.2 | 10 | 10.3 ± 0.2 | 3.3 ± 0.2 |

(2) Similarly to the native fcc-Co polycrystals, the deposition of solution-phase annealed 7.1 nm hcp-Co single crystals (Fig. 8.9a and Table 8.3) gives rise to 2D long-range ordered arrays characterized by center-to-center distance and interparticle gap of 9.8 nm and 2.7 nm, respectively (*Sample Sann* 1) [58]. The increase in the $D_{i\text{-}p}$ of around 1 nm compared to the arrays composed of similar size native NPs is attributed to the presence of larger amount of coating agent, related to the annealing protocol. By slightly increasing the concentration of the colloidal solution, ordered multilayers can also be obtained (Fig. 8.9b).

(3) 2D arrays of hcp-Co single crystals can also result from dry annealing at 350 °C of 2D ordered arrays of as-synthesized Co polycrystals. Such 2D arrays are characterized by NP diameter, $D_{c\text{-}c}$ and $D_{i\text{-}p}$ values equal to 7.0, 10.3 and 3.3 nm, respectively (Fig. 8.9c, Table 8.3). The $D_{i\text{-}p}$ increases after annealing, while the $D_{c\text{-}c}$ remains almost unchanged [23, 58]. NP size decrease is partly attributed to the structural transition of the NPs from the poorly crystalline phase to the hcp-Co single-crystalline phase. As shown in Fig. 8.9d, when the dry annealing is performed on ordered multilayers of Co polycrystals, the assembly keeps their integrity.

Whatever the protocol used is, 2D and thin 3D arrays of Co NPs can be obtained. We show that the characteristics of these organizations can be tuned by varying the mean diameter and the nanocrystallinity of the Co NPs, as well as the mean center-to-center distance between particles and interparticle gap. The high stability of these assemblies, especially in the dry and solution-phase annealing cases, is due to the high thermal stability of dodecanoic acid coating agent.

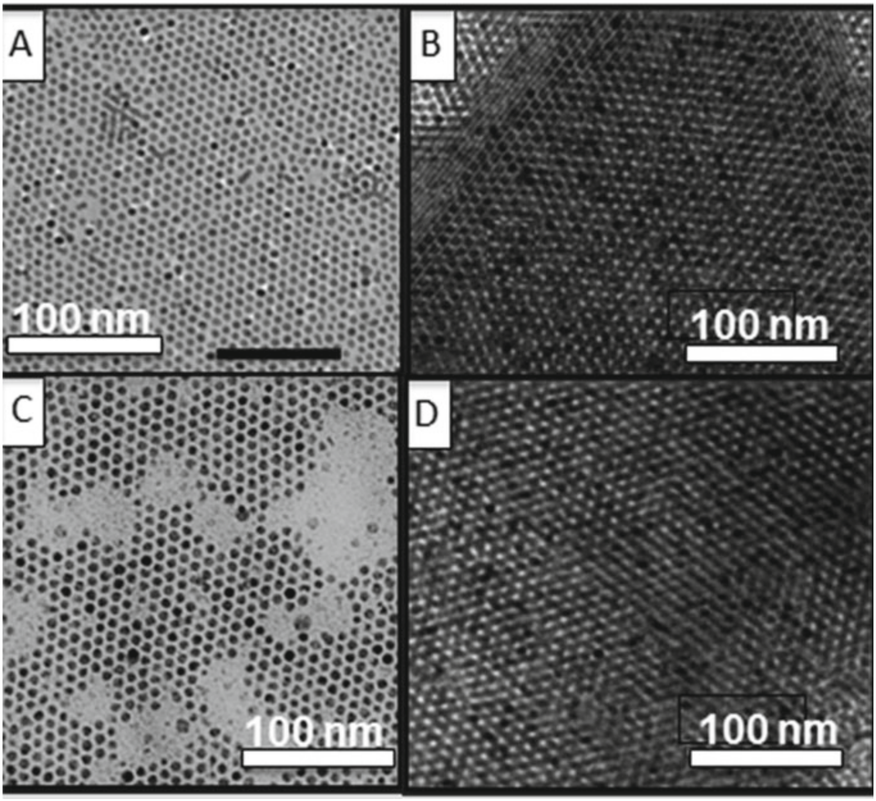

**Fig. 8.9** TEM images of a monolayer (**a**) and a multilayer (**b**) of solution-phase annealed 7.1 nm hcp-Co single crystals obtained by the micellar approach. TEM images of a monolayer (**c**) and a multilayer (**d**) of 7.0 nm hcp-Co single crystals obtained by dry annealing of a native monolayer and multilayer of fcc-Co polycrystals

## 8.6 2D Self-Organizations of Cobalt Nanoparticles Synthesized by Organometallic Approach

The self-assembly process is not dependent of the route used to synthesize the cobalt NPs. As presented above, the 9.2 nm spherical Co NPs coated by oleylamine (OAm) are characterized by low size dispersity (0.6%). By simply depositing a drop of a colloidal solution of these NPs dispersed in toluene, onto amorphous carbon substrates, they self-organize in a long-range 2D hexagonal ordering (Fig. 8.10a) and thin 3D assemblies. When a concentrated solution is allowed to slowly evaporate on graphite substrate, well-developed supercrystals sitting on their larger flat facets are observed. (Fig. 8.10b, c). This is characteristic of the formation of the so-called supercrystals resulting from 3D periodic arrangement of the NPs either in fcc or hcp organization.

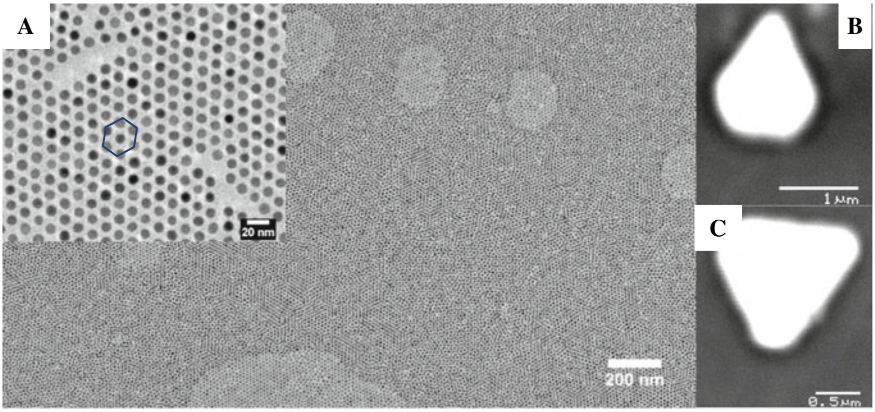

**Fig. 8.10** 9.2 nm spherical cobalt nanoparticles with 6% polydispersity obtained by the organometallic approach self-organized in **a** 2D and thin 3D assemblies as obtained by drop deposition on amorphous carbon. **b** and **c** Superlattices obtained by slow evaporation at room temperature on graphite substrate

As mentioned above, this is due to the attractive Van der Waals interactions between the metallic cores, the "chemical bonds" of self-assemblies resulting from the interdigitation of the ligand molecules (OAm). It should be noticed that from Fig. 8.10a, the deduced interparticle distance is 4.1 nm, which drastically limit the interparticle interaction. As a consequence, no aggregation occurs in the solvent or on the substrates during the deposition process. Indeed, the 2D patterns are purely hexagonal patterns as well as in the thin 3D organization (Fig. 8.10). In case of dipole–dipole interaction, non-close packed superlattices are often observed, which is not the case here. Indeed we can claim that no aggregation occurs in solution due to dipolar interaction.

## *8.6.1 3D Self-Organizations of Cobalt Nanoparticles*

### 8.6.1.1 Control of the Mesoscopic Structure in 3D Assemblies of Co NPs

Dodecanoic acid coated Co NPs synthesized by micellar approach can be used as building blocks to form 2D ordered arrays but also long-range 3D superlattices also called supercrystals. For this aim, an HOPG substrate is horizontally immersed in 200 μl of a highly concentrated colloidal solution ($5.5 \times 10^{-7}$ M) of 7.2 nm. The solvent evaporates under nitrogen flux and the substrate temperature vary from 10 to 45 °C [59]. At 10 °C, TEM study shows the formation of a thin film with a smooth surface (Fig. 8.11a). The diffractogram shows a broad and low intensity Bragg peak indicating the absence of long-range ordering of NPs (Fig. 8.11b). By increasing the temperature from 25 to 45 °C, the film appears cracked and the size of the resulting isolated domains increases with increasing the substrate temperature (Fig. 8.11c,

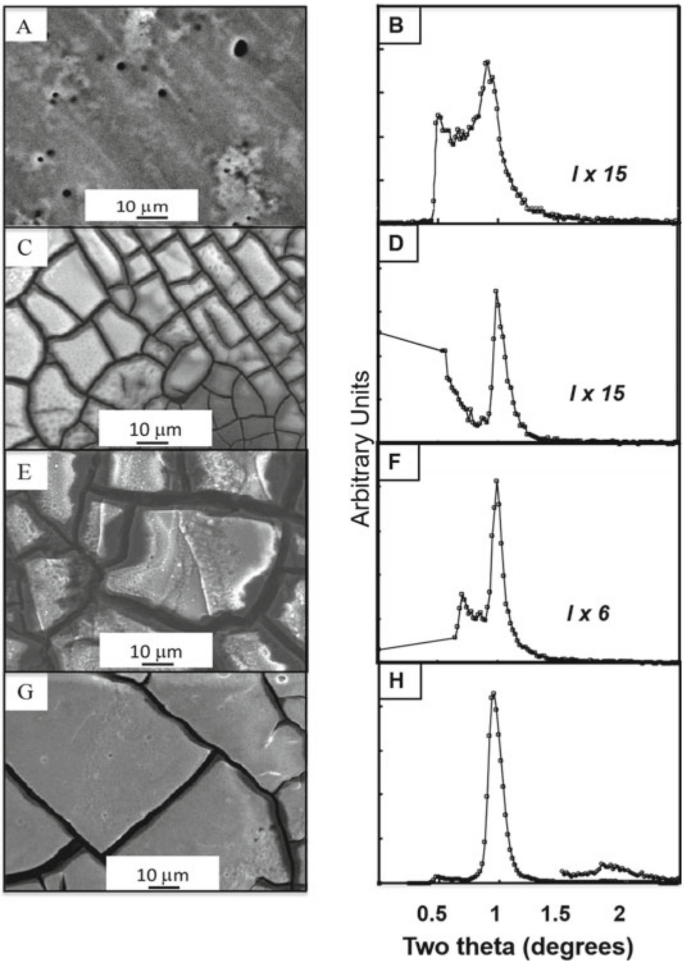

**Fig. 8.11** SEM images obtained by depositing of fcc-cobalt nanoparticles obtained by the micellar approach, on HOPG substrate at various temperatures: **a** 10 °C, **c** 25 °C, **e** 35 °C, **g** 45 °C. **b**, **d**, **f** and **h**, corresponding diffractograms

e, g). For temperatures equal to 25, 35 and 45 °C, the average domain areas are 400, 1000 and 2500 $\mu m^2$, respectively, and their thickness can reach 5 µm. SAXS study clearly indicates a long-range fcc ordering of the NPs [59]. For instance, the X-ray diffraction pattern of the sample obtained at 45 °C (Fig. 8.12) shows various spots which coordinates, when compared to the theoretical values of various structures, correspond to an fcc structure [6]. At 25 °C, the (111) reflection shown in the diffractogram (Fig. 8.11d) is intense and nearly resolution limited (i.e., 0.05 $nm^{-1}$), indicating long-range ordering out of the plane. The interparticle distance is found around 3.60 nm (Table 8.4). By increasing the temperature from 25 to 45 °C, the peak with $\delta q_{1/2}$ decreases from 0.05 to 0.035 and 0.034 $nm^{-1}$, respectively, and become

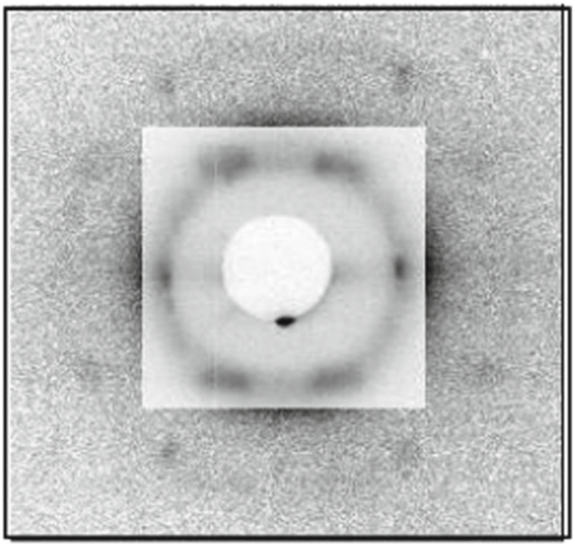

**Fig. 8.12** X-ray diffraction pattern of sample obtained by depositing fcc-cobalt nanoparticles obtained by the micellar approach, on HOPG substrate at 45 °C

**Table 8.4** Structural characteristics of 3D assemblies of Co NPs (7.2 nm) obtained at various temperatures and extracted from the diffractograms presented in Fig. 8.7. $\delta q_{1/2}$: the half width at half maximum; $D_{c\text{-}c}$: center-to-center nanoparticle distance; $D_{i\text{-}p}$: inter-particle distance

| Substrate temperature | $\delta q_{1/2}$ (nm$^{-1}$) | $D_{c\text{-}c}$ (nm) | $D_{i\text{-}p}$ (nm) |
|---|---|---|---|
| 12 °C | 0.190 | 11.75 ± 0.2 | 4.55 ± 0.2 |
| 25 °C | 0.050 | 10.80 ± 0.2 | 3.60 ± 0.2 |
| 35 °C | 0.035 | 10.80 ± 0.2 | 3.60 ± 0.2 |
| 45 °C | 0.034 | 10.60 ± 0.2 | 3.45 ± 0.2 |

increasingly intense (Table 8.4). This behavior clearly evidences an increase in both the size and the coherence length of fcc crystallized domains, i.e., the supercrystals. By increasing the temperature from 25 to 45 °C, the mean interparticle distance decreases from 3.60 to 3.45 nm (Table 8.4) that further evidences the improvement of the mesoscopic ordering.

Hence, by just controlling the substrate temperature, mesoscopic ordering of 3D assemblies of Co NPs can be tuned from disordered to highly fcc ordered assemblies. This behavior is explained by the control of the diffusion of NPs within the solution and on the HOPG substrate.

#### 8.6.1.2 Collective Magnetic Properties in 3D Assemblies of MNPs

Within a NP, small enough to have a single magnetic domain, all atomic spins are aligned in the same direction, and thus, the particle can be considered as a point dipole (or superspin) with a large magnetic moment. Some remarkable phenomena have been observed in MNPs; the most well-known among them being that of superparamagnetism (SPM) of non-interacting NPs, where the magnetic moments of each NPs act independendly [60]. Superparamagnetic NPs have found their use in many fields of applied technology including, but not limited to, biomedicine [61], magnetic resonance imaging [62] data storage [60, 63].

In an assembly of highly concentrated NPs, the materials' magnetic properties can be greatly influenced by the dipolar interactions between NPs. It has been found that at sufficiently high concentrations, the interparticle dipolar interactions can produce "collective states" below a system-dependent transition temperature $T_c$. The observed collective states are almost invariably "disordered" and thus called "superspin glasses" (SSG) as they show many of the phenomenology found in atomic spin glasses [64, 65]. Further increasing inter-particle correlations, the SSG state is predicted to transform into long-range ordered dipolar superferromagnetic (SFM) state. However, a clear-cut experimental evidence of a dipolar SFM state in real 3D NP assemblies has not yet been reported. This is likely due to the stringent geometrical conditions for inducing such a complex state: i.e., long ellipsoidal sample shape, highly ordered fcc or bcc lattice structure and parallel alignment of anisotropy-axis [66, 67]. Due to their structural characteristics, fcc supercrystals of Co NPs are considered as good candidates to display dipolar SFM properties [68, 69]. In the superferromagnetic transition region (from superparamagnetic to superferromagnetic), enhanced magnetocaloric effect is expected, bringing this novel class of material one step close to application in the field of energy efficiency (refrigeration) [70, 71].

#### 8.6.1.3 Collective Magnetic Properties in 3D Fcc Supercrystals of Fcc-Co Polycrystals

The first aim is here (1) to study the effect of the mesoscopic order in 3D assemblies of fcc-Co polycrystals (characterized by a low anisotropy) on the magnetic properties by DC susceptibility measurements. The second one is (2) to study the possibility of superspin glass behavior in the same system by AC susceptibility measurements.

(1) The effect of the structural order of 3D assemblies on magnetic properties is studied by considering highly ordered fcc supercrystals and disordered assemblies. Both ordered and disordered samples are made with the same batch of 7.5 nm fcc-Co polycrystals. The zero field cooled (ZFC) magnetization versus temperature is measured by cooling the sample in zero applied field from 300 to 5 K, applying a field of 20 Oe and then measuring the magnetization as the

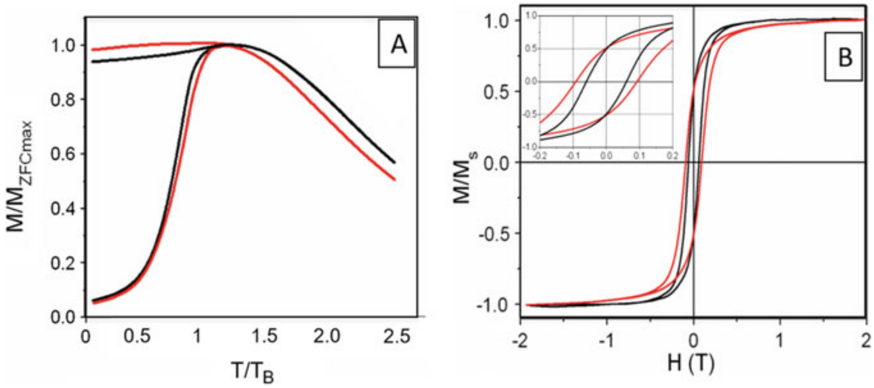

**Fig. 8.13** **A** ZFC magnetization versus T/T$_B$ curves for a supercrystalline film (red) and a disordered 3D assembly of 7.5 nm-Co nanoparticles (black). **B** Magnetization versus field curves at 5 K, normalized to M$_S$ of a supercrystalline film (red) and disordered 3D assembly (black). Inset: Magnification of the low field region

sample is heated. To measure the field cooled (FC) magnetization versus temperature, a field of 20 Oe is applied at 300 K before cooling the sample to 5 K and subsequently measuring the magnetization from 5 to 300 K. The magnetization versus field measurements are carried out at 5 K after zero field cooling of the sample. All magnetic measurements are performed with the applied field parallel to the substrate. Figure 8.13a shows the ZFC and FC curves normalized (ZFC$_{\text{norm}}$ and FC$_{\text{norm}}$) to the blocking temperature, $T_B$, of both the ordered (black) and disordered (red) samples [69].

In ZFC measurements, the sample has been cooled in zero field; hence, there is no net alignment of the superspins at 5 K and the magnetization is close to zero. As the temperature increases, the superspin become progressively "unblocked," aligning toward the field direction and the magnetization increases until reaching a maximum defined as the blocking temperature, $T_B$. Above $T_B$, the behavior is superparamagnetic. That is, the thermal energy increases to such an extend that that the increase dynamic rotation of the superspins prevents alignment in the field direction and the magnetization decreases with increasing temperature. In the FC curve, the magnetization remains almost constant from 5 K to $T_B$. Above $T_B$, the behavior is superparamagnetic and the magnetization decreases with increasing temperature. Whatever the mesoscopic ordering is, $T_B$ does not vary significantly, it value is around 100 K. This is significantly higher value than has previously been observed for dilute systems of similar Co NPs [2] and indicating strong dipolar interactions between the NPs. Besides, the $ZFC_{\text{norm}}$ peak of the disordered sample is significantly enlarged compared to that of the ordered sample. The width of the ZFC peak depends on the distribution of energy barriers, $E_b$, in the assemblies: larger the distribution, broader the peak. The barrier energy is the sum of the anisotropy energy ($E_a = k_a V$ where $k_a$ is the anisotropy constant and $V$ is the NP volume) and the interparticle dipole

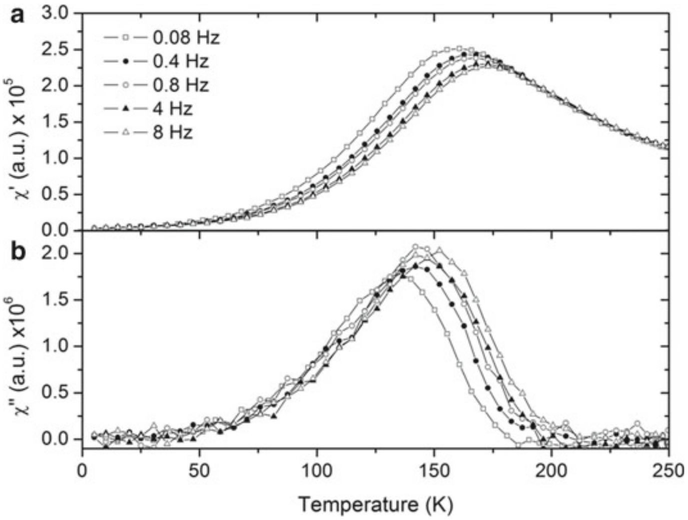

**Fig. 8.14** **a** In-phase and **b** out-of-phase part of the AC susceptibility versus temperature, measured at frequencies between 0.08 and 8 Hz of a supercrystalline film of 8 nm-Co nanoparticles

interaction energy ($E_{dd}$) [72]. Because both ordered and disordered samples are made with the same batch of NPs, we can rule out any effect of NP volume distribution and anisotropy. The behavior observed is explained by the mesoscopic ordering of the assemblies. Indeed, the dipolar interactions are known to be highly directionally sensitive [69]. In highly ordered fcc supercrystal sample, each NP has the same geometrical coordination and the interparticle distance between NPs is uniform. This is not true in the disordered sample. Then, the distribution of $E_{dd}$ and hence $E_b$, in the disordered sample is greater compared to the supercrystal sample, inducing the broadening of the ZFC peak for the disordered sample.

Figure 8.13b shows the corresponding magnetization versus field curves. For the supercrystal sample, the coercive field, $H_c$, is increased compared to that of the disordered sample (900 and 600 Oe respectively). This is attributed to a more collective behavior in the supercrystal sample arising from the long-range ordered fcc structure, which inhibits the rotation of the superspins. Besides, the approach to saturation is slower in ordered sample than in the disordered sample. This last feature in good agreement with the variation of $H_c$, is explained by a higher anisotropy in ordered sample compared to the disordered sample [73, 74].

This result constitutes the first example of collective magnetic properties due to the mesoscopic ordering in 3D assemblies of MNPs.

(2) In order to study the possibility of superspin glass (or SFM) state behavior in fcc supercrystals of 8 nm fcc-Co polycrystals, in addition to DC susceptibility measurements (See below), AC susceptibility measurements are also performed [75]. The latter measurements are required to define the characteristics relaxation times present in the system. The in-phase ($\chi'$) and out-of-phase

($\chi''$) components of the AC susceptibility versus temperature, are measured in a range of AC frequencies varying by 2 decades in magnitude (Fig. 8.14a, b). Both the $\chi'$ and $\chi''$ components show a clear frequency dependence, where the temperature at which the maximum susceptibility is observed ($T_{\text{peak}}$) increases with increasing frequency. $T_{\text{peak}}$ is defined as the temperature at which the relaxation time of the system, $\tau$, is equal to the observation time, $t$, which is related to the measurement frequency by $t = 1/\omega$, where $\omega = 2\pi f$. In order to differentiate between superparamagnetic and superspin glass behaviors, which display both the same frequency dependence in an AC measurement, the change in $T_{\text{peak}}$ with frequency has to be quantitatively analyzed and hence extract a value of $\tau_0$. For a superparamagnet, characterized by negligible dipolar interactions between the magnetic moments, the frequency dependence should follow an Arrhenius law $\tau = \tau_0 e^{\frac{Ea}{k_b T}}$ where is the angular inverse attempt frequency, $E_a$ is the anisotropy energy, and $k_B$ is the Boltzmann constant. By plotting $\log_{10}\tau$ versus $1/T_{\text{peak}}$ and fitting the data to a straight line, the value of $\tau_0$ can be extracted and in this case we find $\tau_0 = 10^{-31}$ s [75]. This unphysically small value indicates that this system cannot be described by simple energy barrier blocking and thermal activation. Actually and analogously to a spin glass, the magnetic response is also influenced by interparticle interaction we have to take into account. In spin glass systems, the dynamic behavior shows a critical slowing down, and hence, the characteristic relaxation time diverges to a finite static glass temperature $T_g$, according to a critical power law $\tau = \tau * (T_{\text{peak}}/T_g{}^{-1})^{-z\nu}$, where $\tau*$ is the relaxation time of an individual NP moment and $z\nu$ is a critical exponent. $T_g$ is taken as the maximum in the DC ZFC magnetization curve. Fitting the data yields $\tau* = 10^{-9\pm3}$ s and $z\nu = 12 \pm 2$. This value of $\tau*$ is in good agreement with values found for spin glasses, and $z\nu$, although slightly high, is also compatible within error to that expected for spin glasses [76–78].

Spin glass and superspin glass materials are known to show aging and memory effects, which can be demonstrated by a simple DC magnetization experiment. The sample is zero field cooled from above $T_g$ to a temperature $T_s$ typically equal to 0.7 $T_g$ where a waiting time of $t_w = 104$ s is imposed before continuing cooling down to low temperature. A small field is then applied and the magnetization is measured on heating. A deviation from the reference ZFC curve (with no stop during cooling) is observed at $T_s$, which is known as a "memory dip," so-called as the system has "remembered" the relaxation toward a zero magnetization value (aging) that occurred during the cooling process.

The results of these AC and DC susceptibility investigations provide strong evidence for superspin glass behavior in long-range ordered fcc supercrystals made of low anisotropy 8 nm fcc-Co polycrystals.

#### 8.6.1.4 Collective Magnetic Properties in Fcc Supercrystals of Hcp-Co Single Crystals

The aim is here to investigate the effect of fcc supercrystals anisotropy on the superspin glass behavior and the possibility for these systems to undergo a transition toward a dipolar SFM state. For this aim, 3D fcc supercrystals of Co polycrystals are submitted to the same thermal treatment used to anneal the 2D ordered arrays, at 250, 300 and 350 °C [23]. SEM study (Fig. 8.15a, c, e, g) indicates that heating process induces the formation of cracks in the supercrystalline film. The beginning of the formation of cracks is observed at 250 °C (Fig. 8.15c). With increasing the temperature, the process is progressively intensifying to give rise, at 350 °C, to isolated domains (Fig. 8.15g). GISAXS study clearly indicates that, whatever the heating temperature is, the fcc superstructure is maintained but not only. We observe both (1) a progressive decrease of the width at half maximum (δ1/2) of the first-order (111) Bragg peak and (2) an increase in the second-order reflection intensity (Fig. 8.15b, d, f, h and Table 8.5). This clearly indicates an increase in the coherence length of the fcc supercrystals. Besides, the interparticle distance between NPs progressively decreases from 3 to 2.2 nm (Table 8.5). This result shows that we are able to control both the crystalline structure of Co NPs and their 3D superstructure. Hence, heating the fcc supercrystals at 350 °C allows the formation of long-range ordered fcc supercrystals composed of hcp-Co single crystals.

The thermal treatment performed on the fcc supercrystals induces drastic changes in the magnetic behavior [11]. As shown in Fig. 8.16a–d, the blocking temperature, $T_B$, progressively increases from 112 K for the native sample to 280 K for the sample annealed at 350 °C. This behavior is mainly explained by the crystallographic transition from almost amorphous NPs to hcp-Co single crystals. After the annealing at 250 °C, the normalized ZFC peak to the $T_B$ (Fig. 8.16e) is broadened compared to the native sample. At this temperature, the crystallographic transition is not complete as evidenced by electron diffraction study, leading to a distribution of the anisotropy in the sample and then to a distribution of the barrier energies. Annealing performed at higher temperature, 300 and 350 °C, induces a progressive narrowing of the $ZFC_{norm}$ peak until the native width is recovered. This behavior is attributed to the crystallographic transition that is complete at 350 °C.

The AC susceptibility as a function of temperature and frequency shows usual “critical slowing down” behavior indicating the existence of collective states below $T_c$ in all fcc supercrystals [79]. Using the Vogel-Fulcher model for weakly interacting systems, the particle anisotropy energy $E_a$ and the effective temperature (related to the interaction energy between NPs) are extracted. As a general trend, the “interaction-to-anisotropy” energy ratio becomes larger with heating of the sample, i.e., with both improving Co nanocrystallinity and decreasing the interparticle gap. Such a behavior is favorable for the formation of a dipolar SFM state.

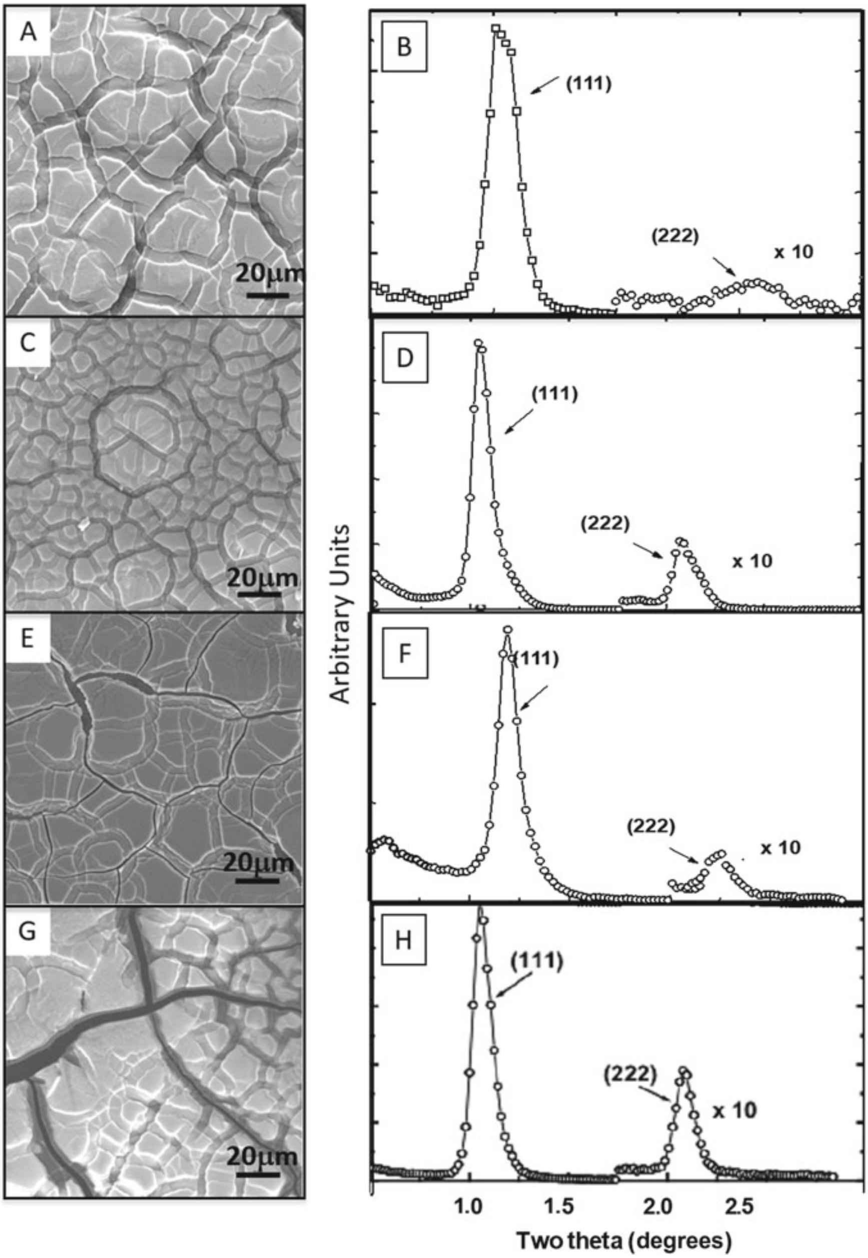

**Fig. 8.15** SEM images of a supercrystalline film (thinner region) of 7.5 nm Co nanoparticles obtained by the micellar approach, not annealed (**a**), annealed at 250 °C (**c**), at 300 °C (**e**) and at 350 °C (**g**). **b**, **d**, **f** and **h** Corresponding diffractograms

**Table 8.5** Structural and magnetic parameters extracted from the GISAXS patterns, the ZFC magnetization curves and the hysteresis. $\delta q1/2$: the half width at half maximum; $D_{c\text{-}c}$: center-to-center NC distance; $D_{i\text{-}p}$: border to border distance of NCs considering a NC size of 7.5 nm; $T_B$: blocking temperature; $M_s$: saturation magnetization; Msnat/Msann: ratio of native $M_s$ to annealed $M_s$; $H_c$: coercivity

| Sample | $D_{c\text{-}c}$ (nm) | $D_{i\text{-}p}$ (nm) | $T_B$ (K) |
|---|---|---|---|
| $Co_{fcc}$ (*Native*) | 10.5 ± 0.1 | 3.0 ± 0.5 | 112 ± 3 |
| $Co_{hcp}$ (*Annealed at* 350 °C) | 9.7 ± 0.1 | 2.2 ± 0.5 | 280 ± 3 |

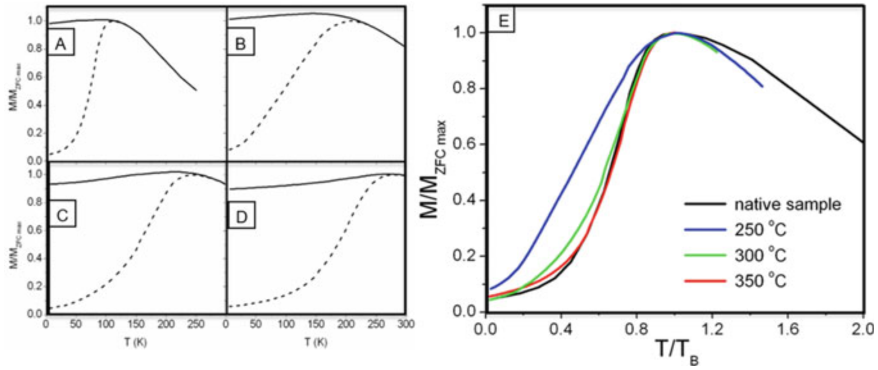

**Fig. 8.16** FC (full lines), and ZFC (dashed lines) magnetization versus $T$ curves of a supracrystalline film of **a** native and annealed at **b** 250 °C, **c** 300 °C, **d** 350 °C. **e** Corresponding ZFC magnetization versus $T/T_B$ curves

## 8.7 Theory of Self-Organization of Magnetic Nanoparticles Under Magnetic Field

The application of a magnetic field during the evaporation leads to the formation of mesostructures. Thus, when the field is parallel to the substrate, chain and columns made of magnetic NPs are observed. The appearance of these structures is surprising, since chains are usually only observed for high dipolar parameters which is defined as the ratio between the magnetic dipolar and thermal energy. Thus, for the maghemite NPs of 10 nm coated with octanoic acid, the dipolar parameter is 0.69 compared to a threshold of 4 where chain formation is usually observed. However, for these NPs, chains are well observed. Brownian dynamics simulations have shown that the mesostructures can be attributed to an interplay of dipolar and van der Waals interactions between the NPs [80, 81]. This also explains why these mesostructures may disappear when ligands with longer alkyl chains such as dodecanoic acid are used. In this case, the van der Waals attraction is reduced due to the larger contact distance between the particles and cannot participate in the mesostructure formation.

Mesostructure formation as observed for MNPs has been widely modeled as confined Stockmeyer fluid in gas–liquid coexistence. The Stockmeyer potential is made of the two terms essential for the mesostructure formation as discussed above: a Lennard–Jones term describing the van der Waals attraction and a magnetic dipole potential. This fluid is confined between two walls describing the film, which is formed during the evaporation. The mesostructure formation is interpreted as a coexistence of a gas and a condensed phase made of the colloidal particles. The condensed phase forms the mesostructures observed in the experiments.

The confined Stockmeyer potential is completely described by five parameters: the dipole strength $\mu$, the density $\rho$, the temperature $T$, the film thickness $L$ and the field strength $H$. These parameters are usually expressed in reduced units. To observe mesostructures, a large number of particles up to 12,000 have to be used. The long-range dipole interaction must be correctly handled using Ewald sums. Several Monte Carlo simulation studies have been carried out for this system and we will summarize the principal results [7, 81–84].

In the literature [85–98], usually particles with high dipole moments are studied by simulations studied have. Thus, the cluster distribution and spacing has been studied for low-density systems made of dipolar hard spheres in a slit geometry [93, 94]. Also the orientational order of dipolar soft spheres has been investigated showing an enhancement of ferroelectric order due to confinement [95, 96].

Concerning mesostructure formation, we will first discuss the simulation results for Stockmeyer fluids when a *field parallel to the film* is applied. Figure 8.17a shows the formation of an array of regularly spaced columns of similar diameter at a height of $L = 10$ [83]. For higher dipoles, the same number of columns is observed, but the particles form an ordered assembly of body-centered tetragonal type. When the height is larger than 10, the diameter of the columns stay close to the value observed for $L = 10$, which leads to the formation of several layers of columns (Fig. 8.17b). When the height is smaller than 10, the columns appear flattened (Fig. 8.17c). When diluted NP solutions are used, the formation of one layer of columns is observed as in Fig. 8.17a. For concentrated solutions corresponding to the case in Fig. 8.17b, several layers of columns are obtained.

The self-organization of magnetic NPs has also widely been studied in the case of *a field perpendicular to the film* [7, 82]. This case is fundamentally different from the parallel one previously discussed. This is explained in the following. The dipoles of the MNPs follow the field direction, which leads to a layer of dipoles pointing in the same direction at the surface of the evaporation film. The aligned dipoles repel each other, which would lead to a separation of the NPs. On the other hand, the NPs are attracted for example by short-range van der Waals attractions as mentioned above. This interplay of short-range attraction and long-range dipolar repulsion leads to the formation of pattern such as hexagonal arrays of columns or labyrinths. This phenomenon can be described by a free energy approach taking into account the repulsion between the aligned dipoles and the energy corresponding to the surface

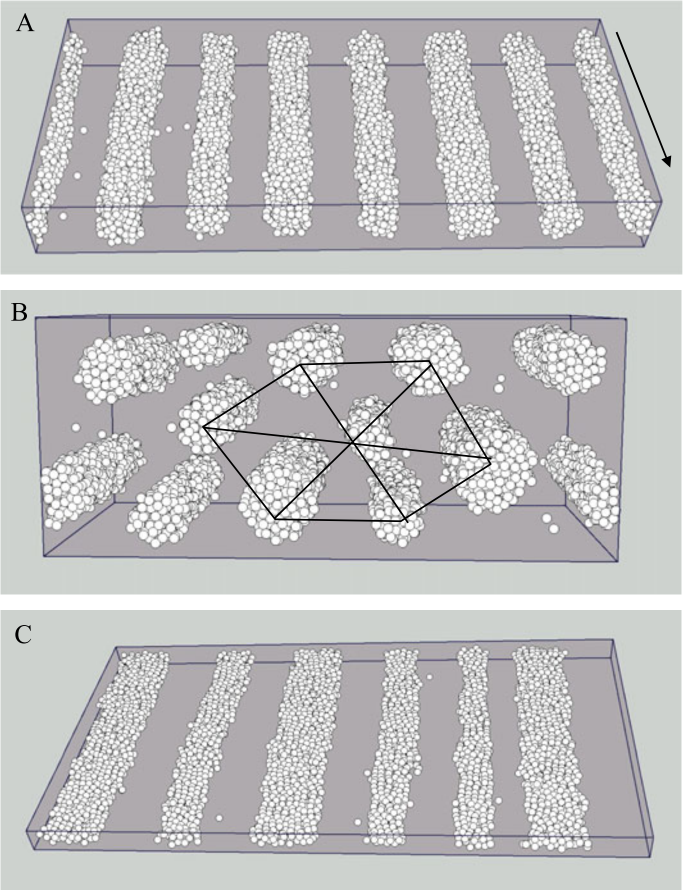

**Fig. 8.17** Snapshots of configurations for a confined Stockmayer fluid at $\mu = 2.0$, $\rho = 0.2$, $T = 1.25$, and $H = 20$. **a** $L = 10$, **b** $L = 27$, **c** $L = 4$

created by the pattern. This approach has been widely applied [99–102] and leads to the following general results: the pattern size such as the radius of columns and the width of labyrinth decreases with the magnetic field strength to reach saturation at high field strength. The ratio of the pattern size and height decreases with the height. A transition between different kinds of patterns is not induced by a change in pattern height or field strength. These transitions are mainly determined by the volume fraction defined as the ratio of the volume occupied by the magnetic phase to the total volume of the film. The self-organization of MNPs in a perpendicular field has also been studied by Monte Carlo simulations using a confined Stockmeyer fluid in the gas–liquid coexistence [7, 103]. System parameters have been chosen close to cobalt NPs coated with dodecanoic acid. The decrease of the pattern size with field strength is in good agreement with the results from free energy approaches

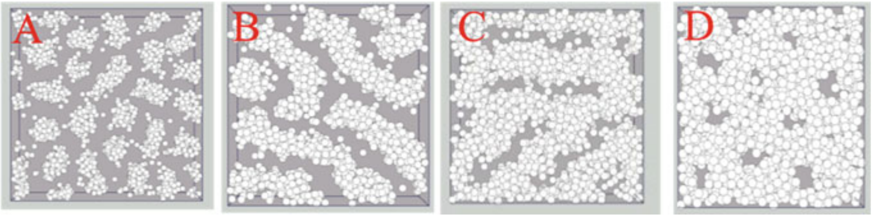

**Fig. 8.18** Snapshots of configurations for a confined Stockmayer fluid at $\mu = 2.0$, $T = 1.25$, $L = 10$ and $H = 30$. **a** $\rho = 0.1$, **b** $\rho = 0.3$, **c** $\rho = 0.4$, **d** $\rho = 0.5$

[102]. Also in the simulations, the volume fraction appears the key parameter for the formation of various patterns [7, 103]. At low volume fractions, only arrays of columns are observed (Fig. 8.18a). For volume fractions close to 0.3, columns and labyrinthine patterns coexist. At even higher volume fraction, a pure labyrinth appears (Fig. 8.18b). At higher volume fractions, two void structures were observed for the first time by simulations. At volume fractions larger than 0.7, a void structure made of elliptical-like holes is obtained (Fig. 8.18c), while from a volume fraction of 0.83 voids with circular base appear (Fig. 8.18d). These void structures were also found in experiments with cobalt NPs at the volume fractions predicted by the simulations [7].

Some years ago, a novel “gel-like” phase was experimentally reported in colloidal suspensions and granular media obtained by *application of an electric field* [101, 104]. These void structures were observed at very low-density $\rho\sigma^3$ between 0.006 and 0.1. To investigate self-organizations at these densities, systematic Monte Carlo simulations were carried out varying the confinement, the short-range interactions and the dipolar moment [84]. Only isolated particles or single chains for large dipoles have been observed at very low density, but no evidence for a void structure was found. It is interesting to note that for larger dipoles, the end of the columns close to the confining walls become broadened. This is explained by the repulsion between the parallel dipoles and has been experimentally observed on ferrofluid emulsions [100, 105].

Using purely repulsive short-range interactions such as hard-sphere repulsion or the Weeks-Chandler-Anderson potential usually leads to the suppression of pattern formations such as columns or voids (see Fig. 8.19a–c). This is in good agreement with observation cited above that the van der Waals interactions are crucial for the formation of pattern.

Surprisingly using bulk-like boundary conditions, we observed the formation of columns even with dipolar hard spheres (Fig. 8.19d). We called this novel unattended phenomenon dipolar assembly with repulsive coupling (DARC). Two conditions must apply for this mesostructure formation without attractive short-range potential. First, quasi bulk-like conditions must exist which are observed for metallic particles in an electric field or magnetic particles in very thick films. Second, the repulsive potential must be very steep [81]. Test calculations have shown that so steep potential may for example apply for NPs stabilized by electrostatic potential.

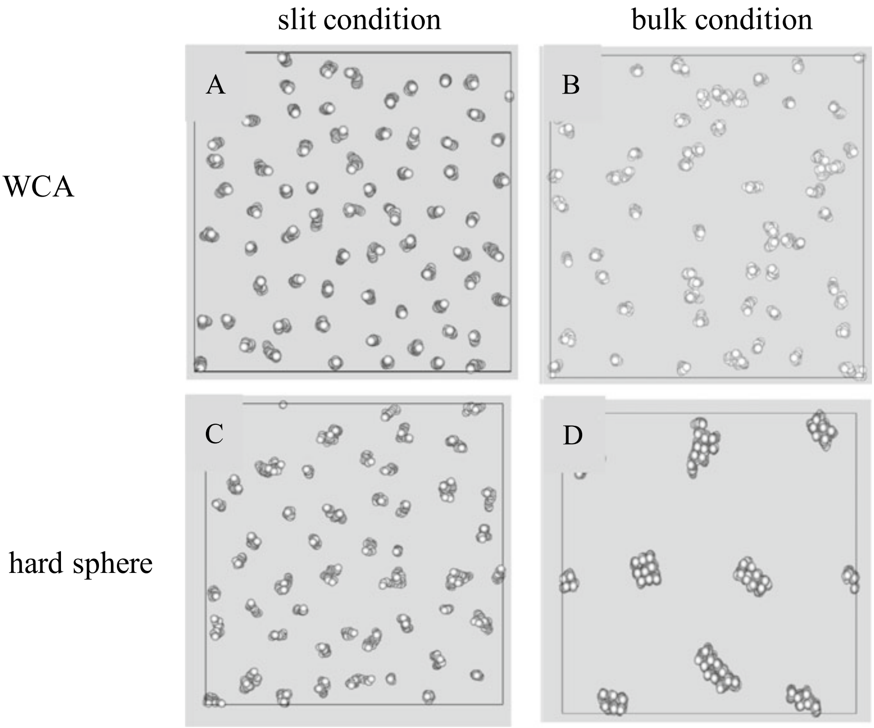

**Fig. 8.19** Snapshots of configurations for a confined dipolar fluid at $\mu = 3.0$, $\rho = 0.1$, $T = 1.0$, $L = 20$ and $H = 40$. In the first and second lines, the repulsion corresponds to the Weeks-Chandler-Anderson (WCA) or the hard-sphere potential. On the left side, slit conditions apply for the simulation box, while on the right side, periodic bulk conditions are used

## 8.8 Conclusion

In this chapter, we show that both micellar and organometallic approaches allows the formation of uniform spherical Co NPs coated either by dodecanoic acid or **oleylamine**, which size can be tuned from **3.8 to 9.2 nm**. Thanks to an annealing process or directly after the synthesis, they are characterized by a hcp crystallinity. Due to their high stability against oxidation and coalescence, these MNPs self-organize into long-range ordered 2D and 3D superlattices. Magnetic properties evidence both the NP crystallinity effect as well as the mesoscopic ordering effect in the 3D supercrystals. We show that there are three key factors for a good assembly of NPs: slow evaporation speed, low size dispersity and the choice of a good solvent. For a specific class of solvents such as toluene, NP assembly can be observed within the solution. Monte Carlo simulations and free energy theories are able to predict the size and type of patterns appearing during the evaporation of a solution of MNPs. They show the importance of short-range attractive forces for the formation of these structures. However, recent simulations have shown that for particles with a steep repulsive potential such additional short-range attractive forces might not be necessary for pattern formation.

**Acknowledgements** The research leading to these results has been supported by a grant ANR-CE08-007 from the ANR French Agency.

## References

1. I. Lisiecki, From the Co nanocrystals to their self-organizations: towards ferromagnetism at room temperature. Acta Phys. Pol. A **121**, 426–433 (2012)
2. A.M. Kalsin, M. Fialkowski, M. Paszewski, S.K. Smoukov, K.J.M. Bishop, B.A. Grzybowski, Electrostatic self-assembly of binary nanoparticle crystals with a diamond-like lattice. Science **312**(80), 420–424 (2006)
3. M.A. Boles, M. Engel, D.V. Talapin, Self-assembly of colloidal nanocrystals: from intricate structures to functional materials—chemical reviews (ACS Publications). Chem. Rev. **116**, 11220–11289 (2016)
4. A. Demortière, C. Petit, First synthesis by liquid−liquid phase transfer of magnetic CoxPt100-X nanoalloys. Langmuir **23**, 8575–8584 (2007)
5. S. Sun, C.B. Murray, D. Weller, L. Folks, A. Moser, Monodisperse FePt nanoparticles and ferromagnetic FePt nanocrystal superlattices. Science **287**(80), 1989–1992 (2000)
6. I. Lisiecki, P.-A. Albouy, M.-P. Pileni, Face-centered-cubic "supracrystals" of cobalt nanocrystals. Adv. Mater. **15**, 712–716 (2003)
7. C. Salzemann, J. Richardi, I. Lisiecki, J.-J. Weis, M.P. Pileni, Mesoscopic void structures in cobalt nanocrystal films formed from drying concentrated colloidal solutions. Phys. Rev. Lett. **102**, 144502 (2009)
8. M. Gauvin, N. Yang, E. Barthel, I. Arfaoui, J. Yang, P.A. Albouy, M.P. Pileni, Morphology, nanocrystallinity, and elastic properties of single domain ε co supracrystals. J. Phys. Chem. C **119**, 7483–7490 (2015)
9. J.J. Urban, D.V. Talapin, E.V. Shevchenko, C.R. Kagan, C.B. Murray, Synergism in binary nanocrystal superlattices leads to enhanced P-type conductivity in self-assembled PbTe/$Ag_2$Te thin films. Nat. Mater. **6**, 115–121 (2007)
10. A. Courty, I. Lisiecki, M.P. Pileni, Vibration of self-organized silver nanocrystals. J. Chem. Phys. **116**, 8074–8078 (2002)
11. D. Parker, I. Lisiecki, C. Salzemann, M. Pileni, M. Curie, Emergence of new collective properties of cobalt nanocrystals ordered in Fcc supracrystals : II. Magn. Invest. 12632–12638 (2007)
12. D. Dinega, M. Bawendi, A solution-phase chemical approach to a new crystal structure of cobalt. Angew. Chemie Int. … 1788–1791 (1999)
13. V.F. Puntes, K.M. Krishnan, A.P. Alivisatos, Colloidal nanocrystal shape and size control: the case of cobalt. Science 291(80), 2115–2117 (2001)
14. C.B. Murray, S. Sun, W. Gaschler, H. Doyle, T.A. Betley, C.R. Kagan, Colloidal synthesis of nanocrystals and nanocrystal superlattices. IBM J. Res. Dev. **45**, 47–56 (2001)
15. J.I.L. Park, N.J. Kang, Y.W. Jun, S.J. Oh, H.C. Ri, J. Cheon, Superlattice and magnetism directed by the size and shape of nanocrystals. ChemPhysChem **3**, 543–547 (2002)
16. S. Sun, C.B. Murray, Synthesis of monodisperse cobalt nanocrystals and their assembly into magnetic superlattices (invited). J. Appl. Phys. **85**, 4325 (1999)
17. L. Zadoina, K. Soulantica, S. Ferrere, B. Lonetti, M. Respaud, A.-F. Mingotaud, A. Falqui, A. Genovese, B. Chaudret, M. Mauzac, In situ synthesis of cobalt nanoparticles in functionalized liquid crystalline polymers. J. Mater. Chem., 6988. (2011)

18. L. Meziane, C. Salzemann, C. Aubert, H. Gérard, C. Petit, M. Petit, Hcp cobalt nanocrystals with high magnetic anisotropy prepared by easy one-pot synthesis. Nanoscale **8**, 18640–18645 (2016)
19. C. Petit, M.P. Pileni, Cobalt nanosized particles organized in a 2D superlattice: synthesis, characterization, and magnetic properties. J. Phys. Chem. B **103**, 1805–1810 (1999)
20. I. Lisiecki, M.P. Pileni, Synthesis of well-defined and low size distribution cobalt nanocrystals: the limited influence of reverse micelles. Langmuir **19**, 9486–9489 (2003)
21. S. Costanzo, G. Simon, J. Richardi, P. Colomban, I. Lisiecki, Solvent effects on cobalt nanocrystal synthesis—a facile strategy to control the size of Co nanocrystals. J. Phys. Chem. C **120**, 22054–22061 (2016)
22. C. Petit, Z.L. Wang, M.P. Pileni, Ferromagnetic cobalt nanocrystals achieved by soft annealing approach-from individual behavior to mesoscopic organized properties. J. Magn. Magn. Mater. (2007)
23. I. Lisiecki, C. Salzemann, D. Parker, P. Albouy, M. Pileni, P. Marie, I. Lisiecki, C. Salzemann, M. Pileni, M. Curie, Emergence of new collective properties of cobalt nanocrystals ordered in Fcc supracrystals : I. Struct. Invest. 12625–12631 (2007)
24. M.D. Bentzon, A.R. Thölén, Phase contrast from a regular stacking of equally sized iron-oxide spheres. Ultramicroscopy **38**, 105–115 (1991)
25. M.D. Bentzon, J. van Wonterghem, S. Mørup, A. Thölén, C.J.W. Koch, Ordered aggregates of ultrafine iron oxide particles: “super crystals.” Philos. Mag. Part B **60**, 169–178 (1989)
26. M. Li, Y. Chen, N. Ji, D. Zeng, D.L. Peng, Preparation of monodisperse Ni nanoparticles and their assembly into 3D nanoparticle superlattices. Mater. Chem. Phys. **147**, 604–610 (2014)
27. M. Okuda, Y. Kobayashi, K. Suzuki, K. Sonoda, T. Kondoh, A. Wagawa, A. Kondo, H. Yoshimura, Self-organized inorganic nanoparticle arrays on protein lattices. Nano Lett. **5**, 991–993 (2005)
28. T. Hyeon, S.S. Lee, J. Park, Y. Chung, H.B. Na, Synthesis of highly crystalline and monodisperse maghemite nanocrystallites without a size-selection process. J. Am. Chem. Soc. **123**, 12798–12801 (2001)
29. L. Meng, W. Chen, Y. Tan, L. Zou, C. Chen, H. Zhou, Q. Peng, Y. Li, $Fe_3O_4$ octahedral colloidal crystals. Nano Res. **4**, 370–375 (2011)
30. O. Kasyutich, R.D. Desautels, B.W. Southern, J. Van Lierop, Novel aspects of magnetic interactions in a macroscopic 3D nanoparticle-based crystal. Phys. Rev. Lett. **104**, 1–4 (2010)
31. C. Petit, P. Lixon, M.P. Pileni, Structural study of divalent metal bis(2-ethylhexyl) sulfosuccinate aggregates. Langmuir **7**, 2620–2625 (1991)
32. I. Lisiecki, P. André, A. Filankembo, C. Petit, J. Tanori, T. Gulik-Krzywicki, B.W. Ninham, M.P. Pileni, Mesostructured fluids. 1. $Cu(AOT)2{-}H_2O{-}$isooctane in oil rich regions. J. Phys. Chem. B **103**, 9168–9175 (1999)
33. I. Lisiecki, P. André, A. Filankembo, C. Petit, J. Tanori, T. Gulik-Krzywicki, B.W. Ninham, M.P. Pileni, Mesostructured fluids. 2. Microstructure and supra-aggregation. J. Phys. Chem. B **103**, 9176–9189 (1999)
34. G.N. Glavee, K.J. Klabunde, C.M. Sorensen, G.C. Hadjipanayis, Sodium borohydride reduction of cobalt ions in nonaqueous media. Formation of ultrafine particles (nanoscale) of cobalt metal. Inorg. Chem. **32**, 474–477 (1993)
35. J. Eastoe, T.F. Towey, B.H. Robinson, J. Williams, R.K. Heenan, Structures of metal bis(2-ethylhexylsulfosuccinate) aggregates in cyclohexane. J. Phys. Chem. **97**, 1459–1463 (1993)
36. J.A. Gutierrez, M. Alejandra Luna, N. Mariano Correa, J.J. Silber, R. Darío Falcone, The impact of the polar core size and external organic media composition on micelle–micelle interactions: the effect on gold nanoparticle synthesis. New J. Chem. **39**, 8887–8895 (2015)
37. N.P. Adhikari, X. Peng, A. Alizadeh, S. Ganti, S.K. Nayak, S.K. Kumar, Multiscale modeling of the surfactant mediated synthesis and supramolecular assembly of cobalt nanodots. Phys. Rev. Lett. **93**, 1–4 (2004)
38. Q. Zeng, X. Jiang, A. Yu, G.M. Lu, Growth mechanisms of silver nanoparticles: a molecular dynamics study. Nanotechnology **18**, 35708 (2007)

39. D. Larcher, R. Patrice, Preparation of metallic powders and alloys in polyol media: a thermodynamic approach. J. Solid State Chem. **154**, 405–411 (2000)
40. F. Bonet, V. Delmas, S. Grugeon, R. Herrera Urbina, P.Y. Silvert, K. Tekaia-Elhsissen, Synthesis of monodisperse Au, Pt, Pd, Ru and Ir nanoparticles in ethylene glycol. Nanostruct. Mater. **11**, 1277–1284 (1999)
41. F. Fievet, J.P. Lagier, M. Figlarz, Preparing monodisperse metal powders in micrometer and submicrometer sizes by the polyol process. MRS Bull. **14**, 29–34 (1989)
42. Y.H. Kim, D.K. Lee, H.G. Cha, C.W. Kim, Y.S. Kang, Synthesis and characterization of antibacterial Ag-$SiO_2$ nanocomposite. J. Phys. Chem. C **111**, 3629–3635 (2007)
43. S.I. Cha, C.B. Mo, K.T. Kim, S.H. Hong, Ferromagnetic cobalt nanodots, nanorices, nanowires and nanoflowers by polyol process. J. Mater. Res. **20**, 2148–2153 (2005)
44. R.J. Joseyphus, T. Matsumoto, H. Takahashi, D. Kodama, K. Tohji, B. Jeyadevan, Designed synthesis of cobalt and its alloys by polyol process. J. Solid State Chem. **180**, 3008–3018 (2007)
45. C. Petit, M. Petit, C. Aubert, L. Meziane, H. Gerard, C. Salzemann, Ambient-temperature ferromagnetic cobalt nanoparticles, production method thereof and uses of same (2017)
46. P.N. Pusey, W. Van Megen, Phase behaviour of concentrated suspensions of nearly hard colloidal spheres. Nature **320**, 340–342 (1986)
47. D.A. Kofke, P.G. Bolhuis, Freezing of polydisperse hard spheres. Phys. Rev. E **59**, 618–622 (1999)
48. P.G. Bolhuis, D.A. Kofke, Monte Carlo study of freezing of polydisperse hard spheres. Phys. Rev. E **54**, 634–643 (1996)
49. S. Auer, D. Frenkel, Suppression of crystal nucleation in polydisperse colloids due to increase of the surface free energy. Nature **413**, 711–713 (2001)
50. L.A. Fernández, V. Mart'in-Mayor, B. Seoane, P. Verrocchio, Separation and fractionation of order and disorder in highly polydisperse systems. Phys. Rev. E **82**, 21501 (2010)
51. S.J. Khan, F. Pierce, C.M. Sorensen, A. Chakrabarti, Self-assembly of ligated gold nanoparticles: phenomenological modeling and computer simulations. Langmuir **25**, 13861–13868 (2009)
52. N. Goubet, J. Richardi, P.A. Albouy, M.P. Pileni, How to predict the growth mechanism of supracrystals from gold nanocrystals. J. Phys. Chem. Lett. **2**, 417–422 (2011)
53. N. Goubet, J. Richardi, P.A. Albouy, M.P. Pileni, Which forces control supracrystal nucleation in organic media? Adv. Funct. Mater. **21**, 2693–2704 (2011)
54. K. Butter, P.H. Bomans, P.M. Frederik, G.J. Vroege, A.P. Philipse, Direct observation of dipolar chains in ferro uids in zero eld using cryogenic electron microscopy. Direct **15** (2003)
55. M. Klokkenburg, R.P.A. Dullens, W.K. Kegel, B.H. Erné, A.P. Philipse, Quantitative real-space analysis of self-assembled structures of magnetic dipolar colloids. Phys. Rev. Lett. **96**, 37203 (2006)
56. M. Klokkenburg, B.H. Erné, J.D. Meeldijk, A. Wiedenmann, A.V. Petukhov, R.P.A. Dullens, A.P. Philipse, In situ imaging of field-induced hexagonal columns in magnetite ferrofluids. Phys. Rev. Lett. **97**, 4–7 (2006)
57. J. Richardi, One-dimensional assemblies of charged nanoparticles in water: a simulation study. J. Chem. Phys. **130** (2009)
58. Z. Yang, M. Cavalier, M. Walls, P. Bonville, I. Lisiecki, M.-P. Pileni, A Phase-solution annealing strategy to control the cobalt nanocrystal anisotropy: structural and magnetic investigations. J. Phys. Chem. C **116**, 15723–15730 (2012)
59. I. Lisiecki, P.-A. Albouy, M.-P. Pileni, "Supra" crystal: control of the ordering of self-organization of cobalt nanocrystals at the mesoscopic scale. J. Phys. Chem. B **108**, 20050–20055 (2004)
60. S. Bedanta, W. Kleemann, Supermagnetism. J. Phys. D. Appl. Phys. **42** (2009)
61. A.G. Roca, R. Costo, A.F. Rebolledo, S. Veintemillas-Verdaguer, P. Tartaj, T. González-Carreño, M.P. Morales, C.J. Serna, Progress in the preparation of magnetic nanoparticles for applications in biomedicine. J. Phys. D. Appl. Phys. **42**, 224002 (2009)

62. J.S. Weinstein, C.G. Varallyay, E. Dosa, S. Gahramanov, B. Hamilton, W.D. Rooney, L.L. Muldoon, E.A. Neuwelt, Superparamagnetic iron oxide nanoparticles: diagnostic magnetic resonance imaging and potential therapeutic applications in neurooncology and central nervous system inflammatory pathologies, a review. J. Cereb. Blood Flow Metab. **30**, 15–35 (2010)
63. A. Moser, K. Takano, D.T. Margulies, M. Albrecht, Y. Sonobe, Y. Ikeda, S. Sun, E.E. Fullerton, Magnetic recording: advancing into the future. J. Phys. D. Appl. Phys. **35** (2002)
64. S. Mørup, Superferromagnetic nanostructures. Hyperfine Interact. **90**, 171–185 (1994)
65. P.E. Jönsson, Superparamagnetism and spin glass dynamics of interacting magnetic nanoparticle systems. Adv. Chem. Phys. 191–248 (2004)
66. S. Bedanta, T. Eimiller, W. Kleemann, J. Rhensius, F. Stromberg, E. Amaladass, S. Cardoso, P.P. Freitas, Overcoming the dipolar disorder in dense CoFe nanoparticle ensembles: superferromagnetism. Phys. Rev. Lett. **98**, 10–13 (2007)
67. J.P. Bouchaud, P.G. Zérah, Dipolar ferromagnetism: a monte carlo study. Phys. Rev. B **47**, 9095–9097 (1993)
68. S. Bedanta, W. Kleemann, Supermagnetism. J. Phys. D Appl. Phys. **42**, 13001 (2009)
69. I. Lisiecki, D. Parker, C. Salzemann, M.P. Pileni, Face-centered cubic supra-crystals and disordered three-dimensional assemblies of 7.5 Nm cobalt nanocrystals: influence of the mesoscopic ordering on the magnetic properties. Chem. Mater. **19**, 4030–4036 (2007)
70. S. Hariharan, J. Gass, Superparamagnetism and magneto-caloric effect (MCE) in functional magnetic nanostructures. Rev. Adv. Mater. Sci. **10**, 398–402 (2005)
71. H. Zeng, J. Zhang, C. Kuang, M. Yue, Magnetic entropy change in bulk nanocrystalline Gd metals. Appl. Nanosci. **1**, 51–57 (2011)
72. J. Dormann, L. Spinu, E. Tronc, J. Jolivet, F. Lucari, F. D'Orazio, D. Fiorani, Effect of interparticle interactions on the dynamical properties of $\gamma$-$Fe_2O_3$ nanoparticles. J. Magn. Magn. Mater. **183**, L255–L260 (1998)
73. J. Tuaillon, J.P. Perez, V. Dupuis, A. Perez, Of Iron and Nickel **8853**, 437–438 (1995)
74. J. Filippi, V.S. Amaral, B. Barbara, High-field magnetization curve of random-anisotropy amorphous magnet: observation of a crossover and link to structural short-range order. Phys. Rev. B **44**, 2842–2845 (1991)
75. D. Parker, I. Lisiecki, M.P. Pileni, Do 8 Nm co nanocrystals in long-range-ordered face-centered cubic (Fcc) supracrystals show superspin glass behavior? J. Phys. Chem. Lett. **1**, 1139–1142 (2010)
76. J. Mydosh, Spin Glasses: An Experimental Introduction (Taylor & Francis, London, 1993)
77. P. Svedlindh, P. Nordblad, M.F. Hansen, Spin glass like transition in a highly concentrated Fe-C nanoparticle system **139**, 1999–2000 (2000)
78. M.F. Hansen, P.E. Jönsson, P. Nordblad, P. Svedlindh, Critical dynamics of an interacting magnetic nanoparticle system. J. Phys. Condens. Matter **14**, 4901–4914 (2002)
79. I. Lisiecki, S. Nakamae, Crystalline order effects on the magnetic properties of superlattices made of cobalt nanocrystals. J. Phys. Conf. Ser. **521**, 12007 (2014)
80. Y. Lalatonne, J. Richardi, P.M.P. Van Der, Waals versus dipolar forces controlling mesoscopic organizations of magnetic nanocrystals. Nat. Mater. **3**, 121–125 (2004)
81. Y. Lalatonne, L. Motte, J. Richardi, M.P. Pileni, Influence of short-range interactions on the mesoscopic organization of magnetic nanocrystals. Phys. Rev. E **71**, 11404 (2005)
82. J. Richardi, M.P. Pileni, J.-J. Weis, Self-organization of magnetic nanoparticles: a Monte Carlo study. Phys. Rev. E **77**, 61510 (2008)
83. J. Richardi, M.P. Pileni, J.J. Weis, Self-organization of confined dipolar particles in a parallel field. J. Chem. Phys. **130** (2009)
84. J. Richardi, J.J. Weis, Low density mesostructures of confined dipolar particles in an external field. J. Chem. Phys. **135** (2011)
85. R. Tao, Q. Jiang, Simulation of structure formation in an electrorheological fluid. Phys. Rev. Lett. **73**, 205–208 (1994)
86. A. Satoh, Development of effective Stokesian dynamics method for ferromagnetic colloidal dispersions (cluster-based Stokesian dynamics method). J. Colloid Interf. Sci. **255**, 98–106 (2002)

87. M. Mohebi, N. Jamasbi, J. Liu, Simulation of the formation of nonequilibrium structures in magnetorheological fluids subject to an external magnetic field. Phys. Rev. E **54**, 5407–5413 (1996)
88. J.E. Martin, R.A. Anderson, C.P. Tigges, Simulation of the athermal coarsening of composites structured by a uniaxial field. J. Chem. Phys. **108**, 3765–3787 (1998)
89. J.E. Martin, R.A. Anderson, C.P. Tigges, Thermal coarsening of uniaxial and biaxial field-structured composites. J. Chem. Phys. **110**, 4854 (1999)
90. J.E. Martin, K.M. Hill, C.P. Tigges, Magnetic-field-induced optical transmittance in colloidal suspensions. Phys. Rev. E **59**, 5676–5692 (1999)
91. Z. Wang, H. Fang, Z. Lin, L. Zhou, Simulation of field-induced structural formation and transition in electromagnetorheological suspensions. Phys. Rev. E **61**, 6837–6844 (2000)
92. A.-P. Hynninen, M. Dijkstra, Phase diagram of dipolar hard and soft spheres: manipulation of colloidal crystal structures by an external field. Phys. Rev. Lett. **94**, 138303 (2005)
93. R. Haghgooie, P.S. Doyle, Transition from two-dimensional to three-dimensional behavior in the self-assembly of magnetorheological fluids confined in thin slits. Phys. Rev. E Stat. Nonlinear Soft Matter Phys. **75**, 1–13 (2007)
94. R. Haghgooie, P.S. Doyle, MR fluid structure in quasi-2D. Europhys. Lett. **77**, 18002 (2007)
95. J. Jordanovic, S.H.L. Klapp, Field-induced layer formation in dipolar nanofilms. Phys. Rev. Lett. **101**, 38302 (2008)
96. R.A. Trasca, S.H.L. Klapp, Structure formation in layered ferrofluid nanofilms. J. Chem. Phys. **129** (2008)
97. S.C. Ferreira, C. Castellano, R. Pastor-Satorras, Epidemic thresholds of the susceptible-infected-susceptible model on networks: a comparison of numerical and theoretical results. Phys. Rev. E **86**, 41125 (2012)
98. J. Richardi, M.P. Pileni, Towards efficient methods for the study of pattern formation in ferrofluid films. Eur. Phys. J. E **13**, 99–106 (2004)
99. J. Richardi, D. Ingert, M.P. Pileni, Theoretical study of the field-induced pattern formation in magnetic liquids. Phys. Rev. E **66**, 46306 (2002)
100. M. Ivey, J. Liu, Y. Zhu, S. Cutillas, Magnetic-field-induced structural transitions in a ferrofluid emulsion. Phys. Rev. E **63**, 11403 (2000)
101. A.K. Agarwal, A. Yethiraj, Low-density ordered phase in brownian dipolar colloidal suspensions. Phys. Rev. Lett. **102**, 198301 (2009)
102. V. Germain, J. Richardi, D. Ingert, M.P. Pileni, Mesostructures of cobalt nanocrystals. 1. Experiment and theory. J. Phys. Chem. B **109**, 5541–5547 (2005)
103. M.P. Pileni, Self organization of inorganic nanocrystals: unexpected chemical and physical properties. J. Colloid Interface Sci. **388**, 1–8 (2012)
104. A. Kumar, B. Khusid, Z. Qiu, A. Acrivos, New electric-field-driven mesoscale phase transitions in polarized suspensions. Phys. Rev. Lett. **95**, 258301 (2005)
105. J. Liu, E.M. Lawrence, A. Wu, M.L. Ivey, G.A. Flores, K. Javier, J. Bibette, J. Richard, Field-induced structures in ferrofluid emulsions. Phys. Rev. Lett. **74**, 2828–2831 (1995)